

Eight Young Associations in the Gum Nebula and a Catalogue of CHIRON Standards

ALEXANDRA C. YEP¹, RUSSEL J. WHITE¹, & AZMAIN NISAK¹¹

¹*Astronomy Department, Georgia State University, Atlanta, GA 30303*

(Received June 21, 2024)

Submitted to ApJ

ABSTRACT

We examine 8 young associations in the Gum Nebula to determine their possible connections with cometary globules and to study how external radiation affects circumstellar disks. Using our simple Cluster Finder code, we found the 8 associations (comprising a total of 1873 stars) near cometary globules CG 1, 3, 4, 14, 17, 22, and 30 and dark globule GDC 1. Three of the associations are newly discovered, three have been previously studied in connection with their nearby cometary globules, and two are known but not well studied. The associations are aged 2 – 650 Myr. We analyze the spectral types, radial velocities, and rotational velocities of 284 stars in the associations via comparison with our catalogue of 81 CHIRON spectral standards. We also measure infrared excess, lithium absorption, and H α absorption or emission. Accretor fractions in all five young clusters in our sample are low for their ages, 29 – 0% at 2 – 11 Myr, suggesting external radiation from hot stars at the heart of the Gum Nebula is eroding young stars’ protoplanetary disks early. This may impede the young stars’ abilities to form planets OR constrain planet formation timescales.

Keywords: accretion, accretion disks — circumstellar matter — stars: formation — stars: fundamental parameters — stars: low-mass — stars: pre-main sequence

1. INTRODUCTION

Stars are born in associations or clusters, sometimes within or close to OB associations. Far-ultraviolet radiation in the Gum Nebula is strong enough to have generated at least 32 cometary globules (Gum 1952; Zealey et al. 1983; see Figure 1). At least 13 stars of type B 1.5 or earlier have been found in the region (Reipurth 1983). O-type star γ^2 Vel, about 5 – 10 Myr old and 349^{+44}_{-35} pc away (Apellániz et al. 2008), lies at the edge of the Vela OB2 association, with components $345.4^{+13.4}_{-12.5}$ pc and $383.4^{+17.8}_{-16.7}$ pc away (Franciosini et al. 2018), and a cluster of low-mass stars aged 10 – 20 Myr (Jeffries et al. 2014; Choudhury & Bhatt 2009). Runaway O-type star ζ Pup, possibly \sim 2.5 Myr old and 335^{+12}_{-11} pc away, was likely flung from OB association Tr 10 to the east (Reipurth 1983; Pettersson 2007; Choudhury & Bhatt 2009; Schilbach & Röser 2008). Until 11,000 yr ago (Reipurth 1983), the Vela XYZ progenitor (294^{+76}_{-50}

pc; Caraveo et al. 2001) also shone in the Gum Nebula. Low-mass star formation events appear to have occurred near CG 4, CG 13, CG 22, and CG 30 (Reipurth & Pettersson 1993; Kim et al. 2006; Pettersson 2007; Rebull et al. 2011).

Moderate radiation could dispel or destroy dusty planetary building blocks and limit stars’ planet formation ability and timeframe (Kim et al. 2005; Sabbi et al. 2020; Yep & White 2020). Far-ultraviolet radiation of strength $G_0 = 6.6^{+3.2}_{-2.7}$ is strong enough to have eroded the protoplanetary disks of young stars near cometary globule CG 30 (Kim et al. 2005; Yep & White 2020). In this paper, we search for other associations in the vicinity of other cometary globules to investigate if they also show evidence of early protoplanetary disk dispersal.

In §2 we describe our technique for identifying young stellar associations in the Gum Nebula. In §3 we expand association membership with reference to other catalogues. We analyze CHIRON spectra of 284 young stars in §4 and derive whole-association properties in §5. In §6 we discuss possible effects of the Gum Nebula’s moderate radiation environment. Finally, we summa-

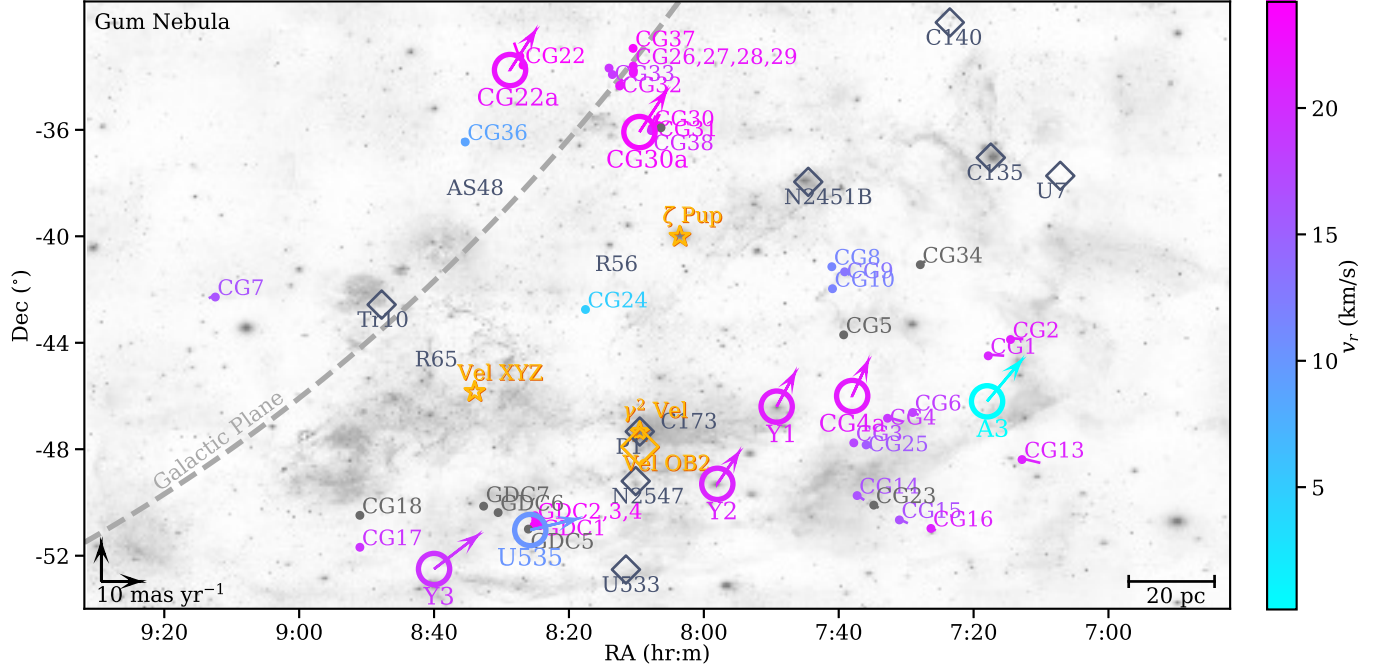


Table 1. Search Parameters and Cuts

CG Name	Cone Search			Cuts				
	RA (°)	Dec (°)	Radius (°)	RA (°)	Dec (°)	Distance (pc)	μ_α (mas yr ⁻¹)	μ_δ (mas yr ⁻¹)
CG 1	109.5	-46.2	3	105.5 – 113	-48 – -44	247.0 – 320.0	-12 – -8	10.5 – 13
CG 3	117.3	-46.4	4	113.8 – 121.8	-50.5 – -44	360.0 – 420.0	-5.2 – -3.8	7.8 – 10
CG 4	114.5	-46.0	3	112 – 114	-48 – -45	405.0 – 450.0	-5 – -2.0	7 – 10
CG 14	119.5	-49.3	4	114.5 – 124.4	-51.0 – -45.5	400.0 – 430.0	-5.9 – -4.8	7.6 – 8.7
CG 17	130.0	-52.5	3	126.3 – 134	-55 – -49.5	320.0 – 370.0	-14.5 – -11.5	9 – 12
CG 22	127.2	-33.8	2	126.2 – 127.8	-35.6 – -33.5	320.0 – 390.0	-8.6 – -5.0	9.5 – 13.1
CG 30	122.4	-36.1	2	121.7 – 123.3	-36.9 – -35.75	340.0 – 390.0	-8.5 – -6.0	9.5 – 12.0
GDC1	126.4	-51.0	4	123 – 131	-55 – -47.5	290.0 – 350.0	-14.5 – -11.5	1.1 – 4.1

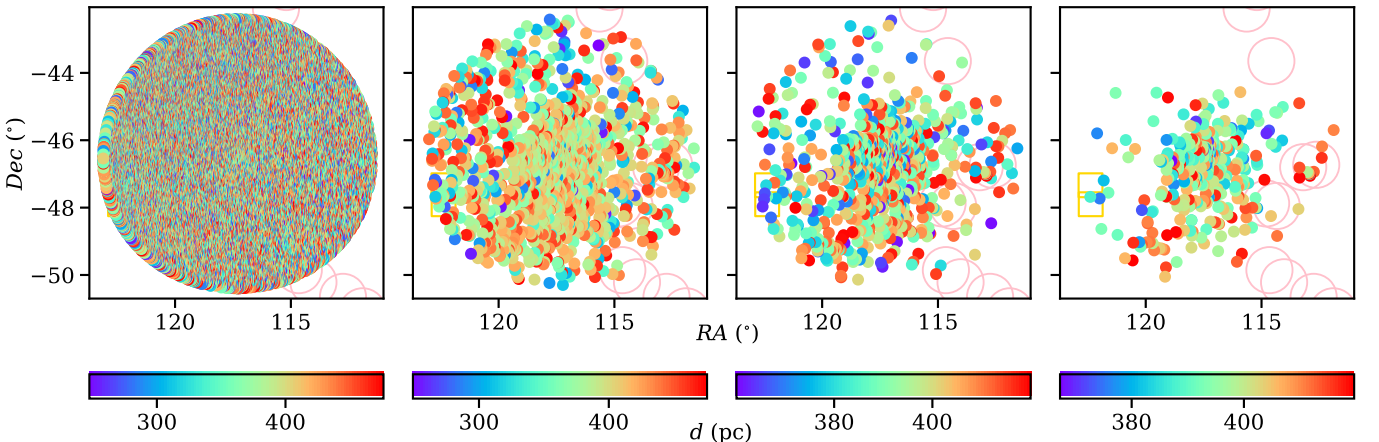


Figure 2. Cluster Finder process, demonstrated on Yep 1. We start with *Gaia* DR2 data with parallax limited to within the Gum Nebula (leftmost panel). We then make proper motion cuts (middle left panel) and refine the distance cuts (middle right panel). Finally, we make error cuts to keep only stars with high-quality astrometry (rightmost panel).

zero. Finally, we crop right ascension and declination to the cluster edges.

Using this method for all 39 CGs and globular dark clouds (GDCs) within 20° of the heart of the Gum Nebula at the projected center of ζ Pup, γ^2 Vel, and Vela XYZ, we have recovered the CG 30 Association and found 7 other associations, or sparse clusters, 7 – 87 pc in diameter (see Figure 3). We include stars down to $V \sim 20$ mag, with V calculated from *Gaia* DR2 magnitudes using the prescriptions of Evans et al. (2018) and Jao et al. (2018) :

$$V = \begin{cases} G + 0.0176 + 0.00686(BP - RP) + 0.1732(BP - RP)^2 & \text{if } BP - RP < 1, \\ 0.97511 \times BP + 0.02489 \times RP - 0.20220, & \text{if } BP - RP \geq 1. \end{cases} \quad (1)$$

Cluster Finder's strengths are its speed and ease of use for finding core members of a cluster or association. In favoring high membership probability over

completeness, we likely exclude less-well-measured and less-bound members, such as runaway stars and some binaries. Our use of proper motions instead of calculated transverse motions may introduce a small degree of incompleteness and contamination. We do not use RUWE, so we may include a few close binary stars in our intended single-star sample. Associated stars further out from the dense center of a cluster or association may evade detection, although Cluster Finder is well suited to handle clusters and associations of all shapes and sizes. Two associations (near CG 4 and CG 30) are sparse and filamentary, and two others (near CG 17 and GDC 1) are significantly elongated along the plane of the Galaxy. We include each association's search parameters and right-ascension-, declination-, distance-, and proper-motion cuts in Table 1.

3. ASSOCIATION CANDIDATES

All of the associations we found using Cluster Finder have been previously identified, at least in part. Three appear in the catalogue of Cantat-Gaudin and Anders

(2020), who found clusters and associations using an unsupervised member classification method based on *Gaia* DR2 and 3-D velocities (see Cantat-Gaudin et al. 2019), and four appear in the catalogue of Kounkel & Covey (2019), who found clusters and associations and so-called strings using unsupervised machine learning. These other catalogues’ search radii tend to be wider than ours. We incorporate these other catalogues’ candidates by applying our slightly expanded cuts (± 5 pc in *Gaia* DR2 parallax-derived distance and ± 0.1 mas yr $^{-1}$ in proper motions) to their membership lists. We then gather distances calculated in Bailer-Jones et al. (2018) for all final association members. We discard candidates with Bailer-Jones et al. (2018) distances >500 pc and distance uncertainties >50 pc.

In naming the 8 associations, we keep the established names of two associations identified in Cantat-Gaudin and Anders (2020). Three associations previously studied alongside their nearby cometary globules inherit the names of those cometary globules. Three associations that appear only loosely in the large strings of Kounkel & Covey (2019) are given new names according to convention, with the lead author’s surname (Yep) and a number.

Here we summarize the identified members of each of the 8 associations, comprising a total of 1873 stars.

3.1. CG 4 Association

We identify 34 stars as members of the CG 4 Association near CG 4. Young stars within and around CG 4 have been studied by Reipurth & Pettersson (1993), Rebull et al. (2011), and Kim et al. (2006), most notably the star RP93 7 = CG-H α 7. We present our own membership list of 34 stars, including RP93 7. We have obtained spectra of 7 of the 34 stars in the CG 4 Association.

3.2. CG 22 Association

We identify 102 stars as members of the CG 22 Association near CG 22. Young stars within and around CG 22 have been studied by Reipurth & Pettersson (1993) and Sahu & Sahu (1992), most notably PH α 92 = Wray 220. The CG 22 Association also corresponds to Theia 31 in Kounkel & Covey (2019). We combine our membership list with that of Kounkel & Covey (2019). Our lists share 63 members. Kounkel & Covey (2019) add 11 members, and we add 27 plus PH α 92. We have obtained spectra of 11 of the 102 stars in the CG 22 Association.

3.3. CG 30 Association

We identify 29 stars as members of the CG 30 Association near CG 30. This association has been studied

by Pettersson (1987), Kim et al. (2005), Yep & White (2020), and others for its distinct, star-forming cometary globule and several young stars, one of which (CG 30 IRS 4) is inside CG 30 itself. We present our membership list of 29 stars, which includes all 14 candidates from Yep & White (2020), 4 of which lack *Gaia* DR2 data. From our previous study, we have Keck I HIRES spectra of 5 stars in the CG 30 Association.

3.4. Yep 1 Association near CG 3

We identify 535 stars as members of the Yep 1 association near CG 3. The association appears loosely in the catalogue of (Kounkel & Covey 2019), constituting 12.4% of Theia 22. Theia 22 may be a conglomerate of several possibly unrelated associations (see also §3.5, so we rename this clustered portion Yep 1. Our membership lists for Yep 1 and Theia 22 share 360 stars. Our cuts keep an additional 104 stars from Theia 22. We contribute another 71 stars. We have obtained spectra of 56 of the 535 stars in Yep 1.

Yep 1 and Yep 2 are spatially close to each other, partially overlap in distance, and have similar space motions. Membership of the two associations has been refined according to a split in proper motion in right ascension μ_α vs. Dec (see Appendix A). It is possible they are two components of one association.

3.5. Yep 2 Association near CG 14

We identify 443 stars as members of the Yep 2 association near CG 14. This association, like Yep 1, appears in the catalogue of Kounkel & Covey (2019) as another portion of Theia 22. Yep 2 contains 11.2% of the stars in Theia 22 and does not have any members in common with Yep 1. The membership lists of Yep 2 and Theia 22 share 219 stars, and our cuts take 198 additional stars from Theia 22. We contribute an additional 26 stars. We have obtained spectra of 46 of the 443 stars in Yep 2.

3.6. Yep 3 Association near CG 17

We identify 297 stars as members of the Yep 3 association near CG 17. This association appears very loosely in Kounkel & Covey (2019) as a westerly 16.2% of the spuriously large Theia 120. Our membership lists for Yep 3 and Theia 120 share 111 stars. Applying our cuts, we take an additional 153 stars from Theia 120 and contribute another 33 stars near the center of Yep 3. We have obtained spectra of 59 of the 297 stars in Yep 3.

3.7. UPK 535 Association near GDC 1

We identify 174 stars as members of the UPK 535 association near GDC 1. Sim et al. (2019) discovered

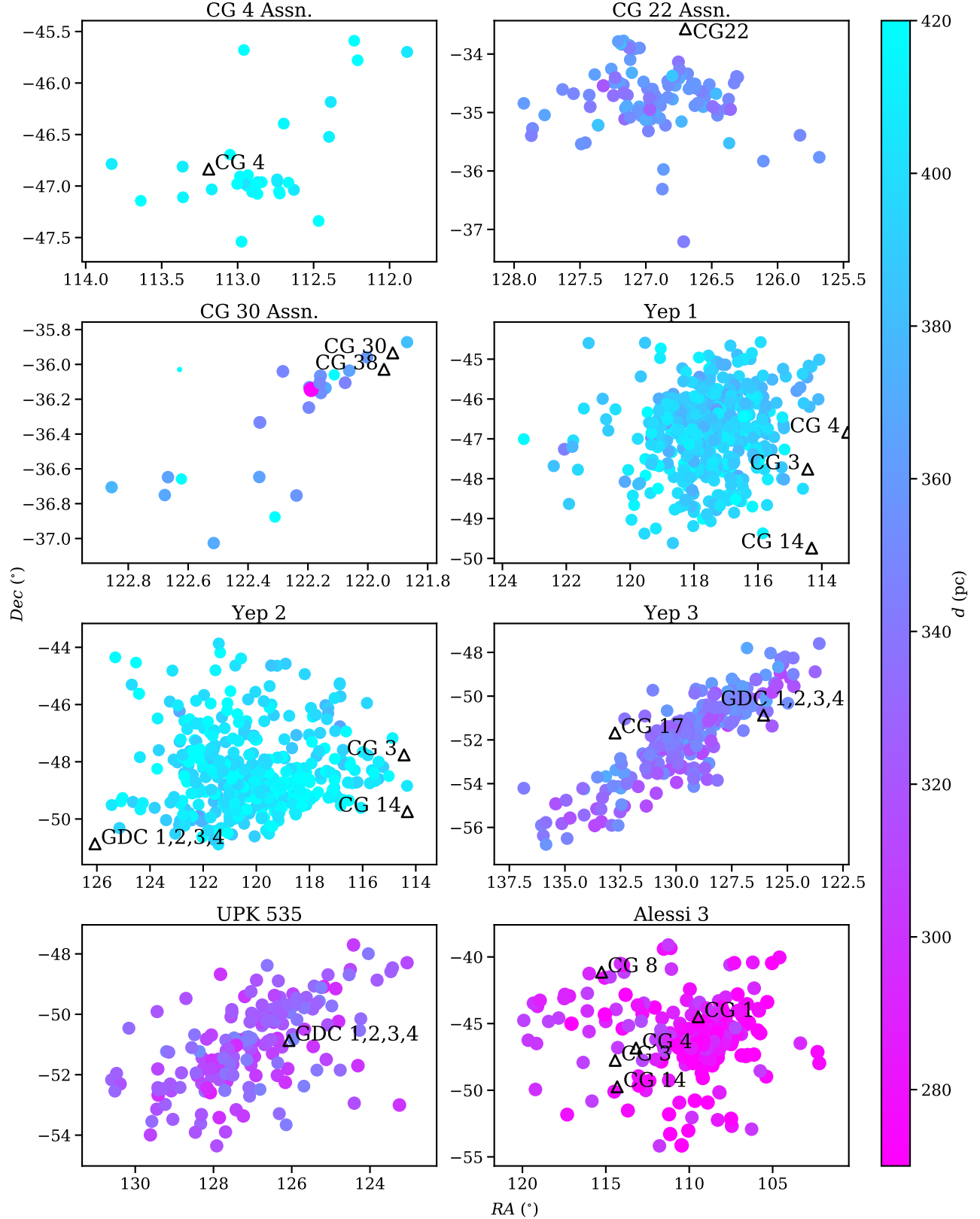


Figure 3. RA vs. Dec of 8 young associations in the Gum Nebula. Cometary globules and dark clouds are marked with black triangles and labeled. The CG 4, 22, and 30 Associations are sparse and may be associated with their nearby cometary globules.

the association via visual inspection of Gaia DR2 data. [Cantat-Gaudin and Anders \(2020\)](#) catalogue the association. Our lists share 86 members. [Cantat-Gaudin and Anders \(2020\)](#) contribute an additional 30 stars, and we contribute 58 stars. We have obtained spectra of 36 of the 174 stars in UPK 535.

3.8. Alessi 3 Association near CG 1

We identify 260 stars as members of the Alessi 3 association near CG 1. [Alessi et al. \(2003\)](#) discovered the association using the statistical method of [Sanders \(1971\)](#) on Tycho-2 data. [Cantat-Gaudin and Anders \(2020\)](#) refined and expanded Alessi 3 membership. Within our 3° search radius, our membership lists agree on 123 stars. [Cantat-Gaudin and Anders \(2020\)](#) contribute an additional 107 stars, and we add 30 stars. We have obtained spectra of 63 of the 260 stars in Alessi 3.

3.9. Association Ages

We estimate association ages by fitting MESA isochrones to the extinction-corrected (see §4.2) single-star main sequences in $Gaia M_G$ vs. corrected $BP - RP$, as illustrated in Fig. 4 ([Paxton et al. 2011, 2013, 2015; Choi et al. 2016; Dotter 2016](#)). Association ages range from 2 to 650 Myr. The isochrones also provide us with a rough estimate for metallicity [Fe/H]. All associations' main sequences are best fit by Solar or supersolar isochrones of 0 – 0.2 dex. Age uncertainties stem from a discrepancy in fitting the main sequence turnoff vs. the bright-for-their-color cool stars. This is a common problem when fitting model isochrones, perhaps due to magnetism, star spots, or other difficult-to-quantify phenomena of cool stars ([Herczeg & Hillenbrand 2015; Asensio-Torres et al. 2019](#)), and perhaps due to blue stragglers ([Beasor et al. 2019](#)). Our isochrone-fit ages are supported by lithium measurements (see §4.5).

4. HIGH DISPERSION OPTICAL SPECTRA

CHIRON is a very stable spectrograph on the SMARTS 1.5 m telescope on Cerro Tololo in Chile ([Tokovinin et al. 2013](#)). Its 4500 – 8500 Å wavelength range includes signatures of youth H α and Li I $\lambda 6708$. In fiber mode, its resolving power $R \approx 25,000$ yields a velocity resolution of 12 km s $^{-1}$.

4.1. Association Observations and Data Reduction

From 2018 Oct 22 to 2021 June, we observed 284 stars in Alessi 3, Yep 1, Yep 2, CG 4 Association, Yep 3, CG 22 Association, and UPK 535 for at least 1 epoch each with the CHIRON spectrograph in fiber mode. We also obtain high-quality (SNR $\gtrsim 100$) spectra of 81 spectral standard stars, publicly available to all CHIRON users

(see Appendix ??).³ Association stars were selected along the apparent single-star main sequence of a *Gaia* $BP - RP$ color vs. BP magnitude diagram (see Fig. 4 for corrected color-magnitude diagrams). We imposed a general brightness cutoff of $V = 13.5$ mag. Twenty-seven dimmer stars with V down to 14.2 mag were also observed before the limit was imposed. We observed each star for up to 1200 s, achieving an SNR of 30 for $V < 9.3$ mag and SNR 30 – 10 for $V 9.3 - 13.5$ mag. Dimmer stars had SNR 5 – 10. Stars with the weakest spectra (particularly PH α 92) were reobserved to bring their SNR into the 10 – 30 range. This SNR of 10 – 30 is sufficient to determine each star's spectral type, radial velocity, stellar rotational speed, continuum excess, H α emission, and Li I $\lambda 6708$ absorption.

CHIRON echelle spectra are reduced by the CHIRON instrumentation team using an IDL pipeline ([Paredes et al. 2021](#)). Spectra are normalized by dividing out the blaze function (see Appendix ??). We focus on 30 well-behaved orders without telluric features and pressure-broadened lines (e.g. Na D), plus the order containing H α .

Stars in the CG 30 Association are too dim to achieve sufficient SNR within our set exposure time limits for CHIRON, so we incorporate CG 30 Association results from [Yep & White \(2020\)](#) derived from spectra from the High-Resolution Echelle Spectrometer (HIRES) on the Keck I telescope in Hawaii.

4.2. Spectral Types, Extinctions, Masses, and Infrared Excesses

Spectral types are determined via visual comparison to our catalogue of CHIRON spectral standards (see Figure 5 and Appendix ??). We assign each star the spectral type of the most similar standard star, and we assign spectral type uncertainties based on the spread of similar standard stars. Spectral types of $V \leq 13.5$ range from K5V to B2V across the 7 spectroscopically measured associations. Spectral types of dimmer stars reach as low as M1.5V, but these stars have SNR < 5 and are not well measured. Two stars in Alessi 3 are giants, types K0III and G9III.

The star CD-46 3194 in the CG 4 Association is a clear double-line spectroscopic binary. Both components are assigned spectral type A6V. The star 2MASS J08443526-5234117 in Yep 3 is a possible double-line or even triple-line spectroscopic binary, but its low SNR ~ 5 renders its binary classification less certain.

To quantify the reddening caused by extinction, we measure *Gaia* color excess $E(BP - RP)$ by comparing

³ https://github.com/alexandrayep/CHIRON_Standards

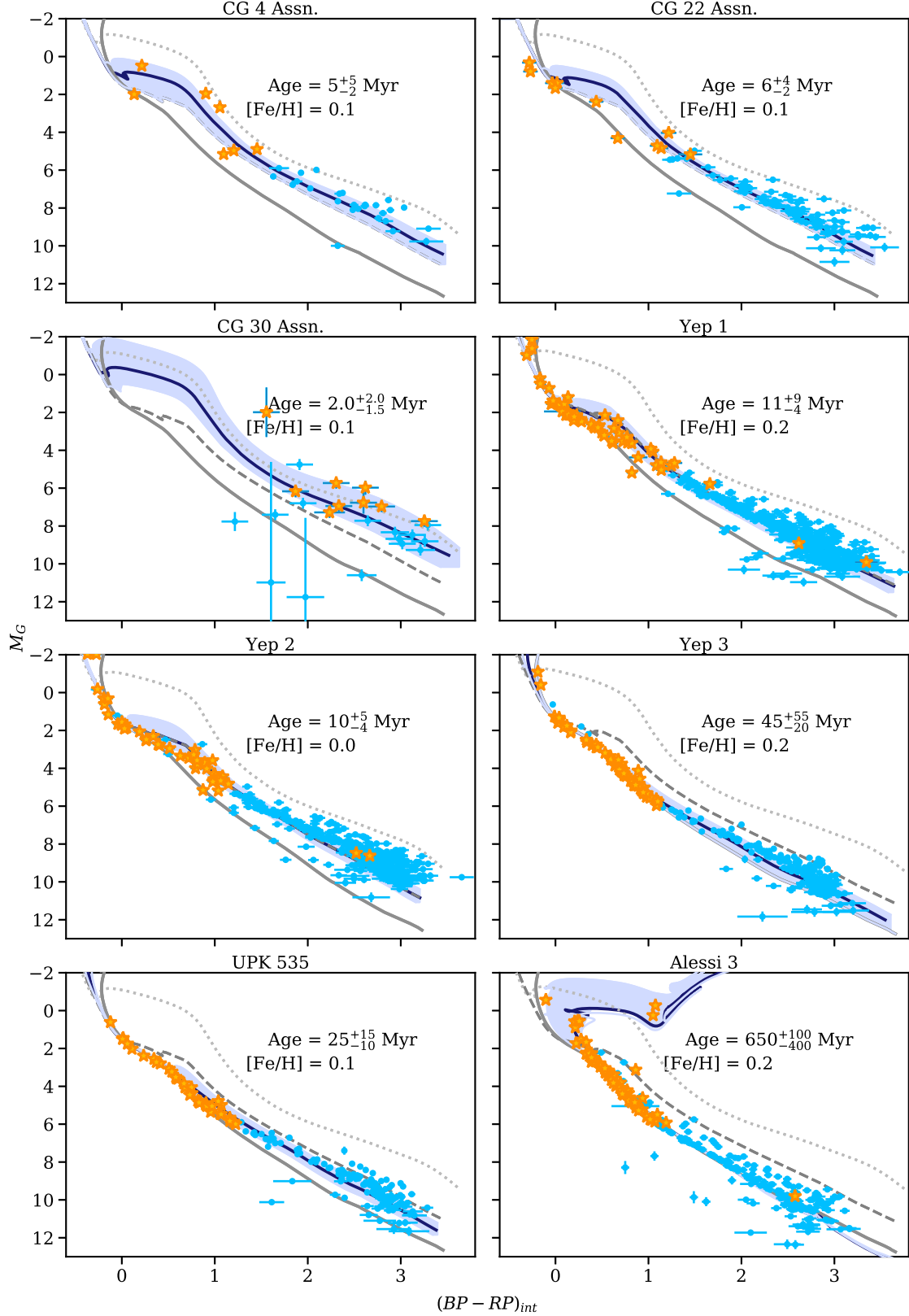


Figure 4. Color-magnitude diagrams. *Gaia* colors are corrected for redenning, and absolute G magnitudes are calculated using distances from (Bailer-Jones et al. 2018) and corrected for extinction. Isochrones are from MESA: dotted gray is 1 Myr, dashed gray is 10 Myr, and solid gray is 100 Myr. Spectroscopically observed stars are plotted as gold stars. Unobserved stars are azure circles. Solid blue isochrones display our age fits, while lilac-shaded regions mark asymmetric age uncertainties. Seven of the 8 associations are fit best by supersolar metallicities, and all are younger than 1 Gyr. Five are $\lesssim 10$ Myr.

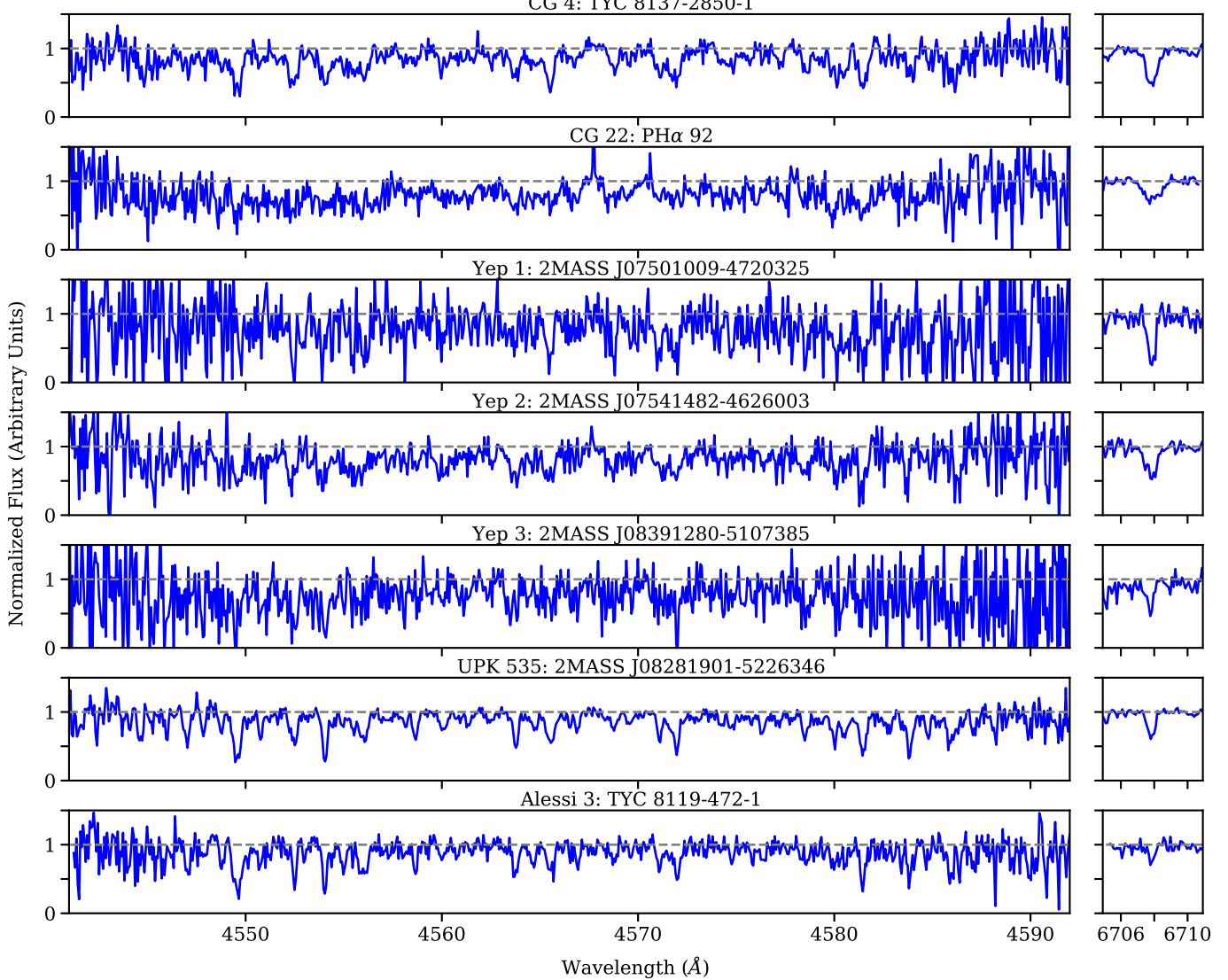


Figure 5. Sample of normalized CHIRON spectra. Order 1 (left panels) is rich in atomic lines and useful for spectral classification and velocity measurements. Order 41 (right panels) contains Li I $\lambda 6708$, present in young stars.

spectroscopically observed stars' apparent *Gaia* colors $BP - RP_{\text{obs}}$ with their spectral types' intrinsic colors $BP - RP_{\text{int,M}}$ according to the dwarf colors of Pecaut & Mamajek (2013).⁴ To avoid biasing results with anomalous red or blue outliers, possibly caused by a variation in local extinction, or skewed by stars with poor photometry or fast rotation that are more difficult to classify, we measure whole-association color excesses $E(BP - RP)_{\text{assn}}$ by taking the flux-error-weighted mean of the middle quartiles of $E(BP - RP)$ values. Stars' *Gaia* color excesses range from -0.661 to 2.378 mag, with median uncertainty 0.052 mag, and associa-

tion means range from 0.036 to 0.349 mag, with a median uncertainty of 0.049 mag, derived from the flux standard deviations of the middle quartiles of each association's $E(BP - RP)$ values. We determine all stars' intrinsic colors $(BP - RP)_{\text{int}}$ by correcting for whole-association reddening: $(BP - RP)_{\text{int}} = (BP - RP)_{\text{obs}} - E(BP - RP)_{\text{assn}}$. Values for $(BP - RP)_{\text{int}}$ span -0.370 – 3.703 mag (see Table 2).

There is no one-to-one relation between *Gaia* color and extinction in BP or RP , but there is an approximate relation between extinction in *Gaia* magnitude G and $E(BP - RP)$ that follows from the PARSEC models: $A_G \approx 2 \cdot E(BP - RP)$ (Andrae et al. 2018). We adopt this approximation to calculate association extinction $A_G \approx 2 \cdot E(BP - RP)_{\text{assn}}$. Extinction values range from 0.072 to 0.698 mag (see Table 4). From these extinc-

⁴ http://www.pas.rochester.edu/~emamajek/EEM_dwarf-UBVIJHK_colors_Teff.txt, version 2021.03.02

tions and Bailer-Jones et al. (2018) distances, we calculate corrected absolute magnitude M_G for each star. Values for M_G span -2.50– 12.36 mag.

Masses can be interpolated from spectral type, ($BP - RP$)_{int}, or *Gaia* absolute magnitude M_G , using the dwarf spectral type or color or magnitude relations of Pecaut & Mamajek (2013), respectively. We use spectral-type-derived masses for all 284 spectroscopically observed stars, color-derived masses for 1515 stars, and absolute-magnitude-derived masses for the 33 stars lacking *BP* or *RP*. Spectral-type-derived-mass uncertainties are propagated from spectral type uncertainties, with lower limit set to 5% of stellar mass to account for uncertainties in choice of stellar model. Spectral-type-derived masses and color-derived masses show an average absolute difference of $\pm 8\%$. Color-derived-mass uncertainties are propagated from color uncertainties, with lower limit set to 8% of stellar mass. Spectral-type-derived masses and absolute-magnitude-derived masses show an average absolute difference of $\pm 11\%$. Absolute-magnitude-derived-mass uncertainties are propagated from G - and distance uncertainties, with lower limit set to 11% of stellar mass. Stellar masses range from 0.12 to $7.30 M_\odot$, with median mass $0.37 M_\odot$ and median uncertainty 8% of stellar mass (see Table 2). Two giant stars in Alessi 3 are assigned the mass of the highest-mass dwarf star in Alessi 3 ($2.75 M_\odot$).

Our stellar mass uncertainties are statistical. Systematic uncertainties, especially because the stars are pre-main sequence, are likely larger.

4.3. Radial Velocities

From the Doppler shift of spectral features, we measure stars' radial velocities. We derive relative velocities using cross-correlation analysis with PyAstronomy's *crosscorrRV* in Doppler mode, comparing each star to 1–11 standards within 2 spectral classes of the target star, across 30 spectral orders. Aberrant orders with velocities differing from the median by $> 3\sigma$ or $> 10 \text{ km s}^{-1}$ are discarded. Most stars with projected rotational velocity $v_{rot} \sin(i) < 100$ keep all 30 orders. For each good order, we compute the intrinsic Doppler uncertainty, lowest for orders with the most spectral features (Butler et al. 1996). We then compute the Doppler-uncertainty-weighted-mean relative velocity from all good orders for each standard. The uncertainty is the sample standard deviation of the good orders' relative velocities, added in quadrature with the uncertainty in the standard's radial velocity. Fifty-eight stars with rapid rotation $> 100 \text{ km s}^{-1}$, few features, and low SNR < 10 have determined radial velocity uncertainties $\sigma_{v_r} > 10 \text{ km s}^{-1}$ and are

considered unmeasured. We successfully measure 226 stars' radial velocities.

Relative velocity is converted to radial velocity relative to the center of the Solar System using each standard's barycentric correction, calculated using the PyAstronomy function *helcorr* (Czesla et al. 2019).⁵ Final radial velocity v_r for each star is the error-weighted mean of the comparison standards' results. Final uncertainty is the greater of the following: the error-weighted-mean error or, usually, the sample standard deviation of the comparison standards' results. Including results for possible spectroscopic binaries, radial velocities range from -60.59 to 101.87 km s^{-1} (see Table 2). Associations' error-weighted-mean radial velocities range from 0.2 to 22.8 km s^{-1} (see Table 4). The median radial velocity uncertainty is 0.52 km s^{-1} .

By the nature of our Cluster Finder search, all stars observed have positions, distances, and proper motions consistent with their associations. They also share signatures of youth Li I $\lambda 6708$ (see §4.5) and H α (see §4.6). Although we targeted stars along the apparent single-star main sequence, one star is clearly a double-line spectroscopic binary, one star is possibly a double-line spectroscopic binary, and 52 stars have radial velocities $> 5 \text{ km s}^{-1}$ discrepant from their association medians (see §5.1). Of these, five stars have serendipitous CHIRON followup observations with radial velocity shifts $> 5 \text{ km s}^{-1}$ confirming their binarity. The remaining 47 stars are treated as single-line spectroscopic binaries in this study.

4.4. Projected Rotational Velocities

We measure each star's rotational broadening relative to the same comparison standards used in the cross-correlation analysis for determining radial velocities (see §4.3). For each spectral order, we artificially broaden each standard using PyAstronomy's *rotBroad* based on Gray (1992), with limb-darkening coefficient $\epsilon = 0.6$, appropriate for optical wavelengths. We derive a relation between the amount of broadening applied to the standard and the Gaussian width of the peak of the standard's autocorrelation function with its unbroadened self. We then measure the width of the peak of the cross-correlation between the target star and the unbroadened standard and use the autocorrelation-derived width vs. broadening relation to determine applied broadening v_b . Each standard has a known or estimated projected rotational velocity v_i . The total measured projected rotational velocity of the target star is a combination of v_b

⁵ <https://github.com/szesla/PyAstronomy>

Table 2. Sample of Each Association's Member Kinematics and Properties

<i>Gaia</i> DR2 Source	Star Name	RA ($^{\circ}$)	Dec ($^{\circ}$)	Parallax (mas)	μ_{α} (mas yr $^{-1}$)	μ_{δ} (mas yr $^{-1}$)	v_r (km s $^{-1}$)	G (mag)	B P (mag)	R P (mag)	V (mag)	Spectral Type	Class	Binary Flag	d (pc)	Mass (M $_{\odot}$)
CG 4 Assn.																
551082639858581824	...	112.23297 -45.5894	2.335 ± 0.076	-3.65 ± 0.15	9.50 ± 0.14	8.998 ± 0.074	7.1 ± 1.7	16.944 ± 0.001 16.848 ± 0.029	15.611 ± 0.005	18.565 ± 0.028	424 $^{+14}_{-13}$	0.243 ± 0.019
5507704230322705408	CD-46 3194	112.39847 -46.5226	2.403 ± 0.033	-4.036 ± 0.065	8.998 ± 0.074	7.1 ± 1.7	9.254 ± 0.001	9.483 ± 0.002	8.919 ± 0.003	9.331 ± 0.007	AIV	1.0	SII $_{\star}$...	411 $^{+5.7}_{-5.5}$	1.830 ± 0.002
550743555050533184	...	112.46667 -47.3395	2.347 ± 0.052	-4.122 ± 0.091	8.24 ± 0.13	...	16.023 ± 0.001	17.525 ± 0.009	14.801 ± 0.003	17.255 ± 0.009	421 $^{+12}_{-10}$	0.404 ± 0.032
550743542986629120	...	112.72733 -47.0519	2.327 ± 0.071	-4.09 ± 0.13	8.82 ± 0.13	...	16.421 ± 0.002	18.281 ± 0.022	15.065 ± 0.010	17.999 ± 0.021	425 $^{+13}_{-12}$	0.248 ± 0.020
5507466770169790464	...	112.98486 -46.90633	2.294 ± 0.036	-4.354 ± 0.082	8.526 ± 0.063	...	15.464 ± 0.011	16.614 ± 0.042	14.382 ± 0.028	16.356 ± 0.041	430 $^{+6.8}_{-6.6}$	0.560 ± 0.045
CG 22 Assn.																
5543404857490433024	...	126.8512 -35.2181	2.824 ± 0.035	-6.930 ± 0.056	10.432 ± 0.052	...	15.139 ± 0.004	16.325 ± 0.020	14.049 ± 0.011	16.066 ± 0.019	350 $^{+6.4}_{-5.4}$	0.528 ± 0.042
554356794575835136	2MASS J08284752-3429298	127.1980 -34.4916	2.726 ± 0.030	-6.820 ± 0.045	11.273 ± 0.048	20.79 ± 0.43	12.277 ± 0.007	12.933 ± 0.025	11.493 ± 0.019	12.695 ± 0.025	KIV	2.0	363 $^{+4.0}_{-3.9}$	0.860 ± 0.060
55437443162225024	...	126.6281 -34.8838	2.774 ± 0.098	-7.10 ± 0.16	10.46 ± 0.17	...	17.240 ± 0.010	19.423 ± 0.039	15.844 ± 0.004	19.132 ± 0.038	358 $^{+13}_{-13}$	1.161 ± 0.013
554353212959451648	...	126.94935 -34.5996	2.790 ± 0.046	-6.985 ± 0.067	11.010 ± 0.067	...	15.423 ± 0.004	16.024	15.151 ± 0.007	17.917 ± 0.023	354 $^{+8.6}_{-6.8}$	0.671 ± 0.074
554351821026552896	...	127.4298 -34.7020	2.822 ± 0.077	-6.41 ± 0.11	11.42 ± 0.13	...	16.526 ± 0.002	18.194 ± 0.024	15.151 ± 0.007	17.917 ± 0.023	351.1 $^{+8.8}_{-8.8}$	0.260 ± 0.021
CG 30 Assn.																
554461816857600320	pha15	122.1950 -36.1313	2.794 ± 0.036	-7.579 ± 0.068	11.451 ± 0.067	21.89 ± 0.20	15.116 ± 0.013	16.259 ± 0.074	13.980 ± 0.033	16.000 ± 0.072	MIV	0.5	354.4 $^{+4.5}_{-4.3}$	0.230 ± 0.043
55446194065523173576	KWW 1863	122.1576 -36.0553	2.774 ± 0.031	-7.400 ± 0.056	12.025 ± 0.056	26.2 ± 3.0	13.584 ± 0.003	14.469 ± 0.004	14.558 ± 0.004	15.004	MIV	350.5 $^{+3.9}_{-3.9}$	0.500 ± 0.038
55446224978996602886	KWW 1953	122.1121 -36.0598	2.210 ± 0.023	-6.14 ± 0.39	12.79 ± 0.40	24.5 ± 3.0	9.655 ± 0.000	9.762 ± 0.001	9.502 ± 0.001	9.675 ± 0.004	M3V	456 $^{+45}_{-45}$	0.370 ± 0.051
5544621741985468416	...	122.0756 -36.1054	2.857 ± 0.054	-7.784 ± 0.097	11.172 ± 0.093	...	16.120 ± 0.011	17.795 ± 0.042	14.813 ± 0.030	17.519 ± 0.041	346 $^{+7.4}_{-6.6}$	0.231 ± 0.035
554460512110973376	...	122.1969 -36.2480	2.833 ± 0.067	-7.44 ± 0.12	11.24 ± 0.11	...	16.277 ± 0.002	18.114 ± 0.024	14.944 ± 0.005	17.833 ± 0.023	349.7 $^{+8.1}_{-8.1}$	0.191 ± 0.025
Yep 1																
553040406255445824	...	115.7942 -47.7632	2.474 ± 0.048	-4.910 ± 0.089	8.463 ± 0.093	...	16.086 ± 0.003	17.454 ± 0.025	14.890 ± 0.006	17.188 ± 0.025	399.7 $^{+7.9}_{-7.6}$	0.380 ± 0.031
55118255711140608	...	118.3498 -48.0738	2.477 ± 0.049	-4.836 ± 0.090	8.76 ± 0.10	...	15.599 ± 0.002	16.952 ± 0.010	14.413 ± 0.004	16.687 ± 0.010	399.3 $^{+5.2}_{-5.2}$	0.396 ± 0.032
551180258446729384	HD 64780	118.3525 -46.9059	2.473 ± 0.030	-4.650 ± 0.052	8.704 ± 0.057	...	9.659 ± 0.000	9.782 ± 0.001	9.582 ± 0.001	9.675 ± 0.004	AIV	1.0	399.8 $^{+4.8}_{-4.8}$	2.18 ± 0.35
5511824493821087040	TYC 8139-3353-1	118.5110 -48.3601	2.464 ± 0.025	-4.738 ± 0.051	8.107 ± 0.050	22.70 ± 0.05	11.912 ± 0.003	11.308 ± 0.008	11.354 ± 0.007	12.094 ± 0.028	G IV	1.0	401.1 $^{+4.1}_{-4.1}$	1.030 ± 0.052
553061993123757522	...	117.2739 -46.5463	2.57 ± 0.12	-4.60 ± 0.25	9.13 ± 0.24	...	18.188 ± 0.002	19.899 ± 0.007	16.895 ± 0.005	19.621 ± 0.005	387.1 $^{+18}_{-18}$	0.233 ± 0.020
Yep 2																
551461362168901632	...	121.9038 -48.5335	2.49 ± 0.12	-5.86 ± 0.24	8.31 ± 0.22	...	17.585 ± 0.002	19.350 ± 0.065	16.233 ± 0.008	19.070 ± 0.063	398 $^{+17.8}_{-18}$	0.226 ± 0.019
551161632190532238536	...	122.5352 -48.0071	2.36 ± 0.15	-5.61 ± 0.27	7.52 ± 0.27	...	18.279 ± 0.003	19.82 ± 0.12	16.845 ± 0.016	15.55 ± 0.12	421 $^{+30}_{-30}$	0.260 ± 0.038
55118399244348273664	...	116.4646 -48.1330	2.342 ± 0.069	-5.35 ± 0.13	8.04 ± 0.14	...	16.941 ± 0.001	18.530 ± 0.033	16.680 ± 0.004	18.257 ± 0.032	422 $^{+13}_{-12}$	0.302 ± 0.024
5511848628186499396	...	117.6447 -47.6280	2.480 ± 0.045	-5.495 ± 0.033	8.436 ± 0.036	...	13.827 ± 0.001	14.511 ± 0.004	13.031 ± 0.003	14.272 ± 0.004	388.5 ± 2.7	0.738 ± 0.059
5511822105044968448	...	118.7004 -48.2438	2.470 ± 0.039	-5.379 ± 0.074	8.611 ± 0.069	...	15.531 ± 0.004	16.620 ± 0.022	14.488 ± 0.008	16.365 ± 0.021	400 $^{+4.6}_{-4.2}$	0.539 ± 0.043
Yep 3																
532168820030950432	TYC 8163-2131-1	129.9593 -51.5401	2.876 ± 0.026	-12.625 ± 0.050	9.199 ± 0.053	-10.15 ± 0.05	9.05	11.888 ± 0.001	11.346 ± 0.003	12.073 ± 0.004	F6V	3.0	SII $_{\star}$...	344.3 $^{+3.2}_{-3.2}$	1.25 ± 0.16
5321625901749892900	TYC 8163-1809-1	129.9765 -51.9052	2.814 ± 0.028	-12.101 ± 0.050	10.536 ± 0.053	12.06 ± 0.16	11.826 ± 0.002	11.263 ± 0.002	11.163 ± 0.002	11.639 ± 0.003	K3V	1.5	326.3 $^{+6.8}_{-6.8}$	0.414 ± 0.033
532163732250617856	2MASS J08405718-5145010	130.2388 -51.7503	2.813 ± 0.059	-12.91 ± 0.11	9.83 ± 0.13	...	16.323 ± 0.002	17.515 ± 0.012	15.201 ± 0.004	17.255 ± 0.012	323.5 $^{+5.1}_{-5.1}$	1.180 ± 0.050
532473737536320512	CD-50 3593	132.3128 -51.401	2.928 ± 0.043	-12.992 ± 0.077	11.482 ± 0.050	...	9.913 ± 0.000	10.069 ± 0.001	9.678 ± 0.002	9.960 ± 0.004	338.3 $^{+4.9}_{-4.9}$	1.67 ± 0.13
5317163813045331968	...	132.4527 -54.9563	2.789 ± 0.074	-12.07 ± 0.15	9.69 ± 0.14	...	15.803 ± 0.001	16.916 ± 0.004	14.695 ± 0.002	16.659 ± 0.004	355.3 $^{+5.1}_{-5.1}$	0.454 ± 0.036
5511531188872004096	...	126.3425 -48.8964	3.041 ± 0.062	-12.44 ± 0.10	2.77 ± 0.10	...	16.325 ± 0.002	17.575 ± 0.013	15.183 ± 0.004	17.314 ± 0.012	326 $^{+6.8}_{-6.8}$	0.414 ± 0.033
532304575612719080	2MASS J07122400-4522466	108.1000 -45.3796	3.369 ± 0.026	-9.342 ± 0.043	11.241 ± 0.046	1.20 ± 0.12	12.266 ± 0.001	12.622 ± 0.002	11.766 ± 0.002	12.416 ± 0.008	G3V	1.0	294.3 $^{+2.2}_{-2.2}$	0.990 ± 0.050
532162590224060	2MASS J07140743-4628549	108.5310 -46.4819	3.559 ± 0.014	-10.246 ± 0.025	12.073 ± 0.032	6.65 ± 0.79	13.165 ± 0.001	13.646 ± 0.003	12.540 ± 0.002	13.417 ± 0.003	K4V	1.0	278.7 ± 1.1	0.730 ± 0.040
5321625902619068	TYC 8162-956-1	127.5688 -51.8860	3.218 ± 0.032	-9.454 ± 0.040	11.754 ± 0.040	-3.1 ± 6.0	9.578 ± 0.000	9.731 ± 0.002	9.336 ± 0.002	9.622 ± 0.005	A2V	1.0	285.0 ± 1.8	1.980 ± 0.099
532266317876677648	...	126.4354 -50.2127	2.994 ± 0.096	-12.71 ± 0.18	2.79 ± 0.19	...	17.428 ± 0.002	18.397 ± 0.029	16.141 ± 0.004	18.724 ± 0.029	274.3 ± 2.0	1.460 ± 0.073
5511531188871310261248	...	123.8186 -48.8964	3.057 ± 0.083	-12.22 ± 0.15	3.87 ± 0.13	...	16.874 ± 0.002	18.322 ± 0.020	15.653 ± 0.004	18.053 ± 0.019	274.1 $^{+8.3}_{-8.8}$	0.264 ± 0.021
551101308181237190680	2MASS J07122400-4522466	108.1000 -45.3796	3.369 ± 0.026	-9.342 ± 0.043	11.241 ± 0.046	1.20 ± 0.12	12.266 ± 0.001	12.622 ± 0.002	11.766 ± 0.002	12.416 ± 0.008	G3V	1.0	294.3 $^{+2.2}_{-2.2}$	0.990 ± 0.050
550973631629124060	2MASS J07140743-4628549	108.5310 -46.4819	3.559 ± 0.014	-10.246 ± 0.025	12.073 ± 0.032	6.65 ± 0.79	13.165 ± 0.001	13.646 ± 0.003	12.540 ± 0.002	13.417 ± 0.003	K4V	1.0	278.7 ± 1.1	0.730 ± 0.040
550872491642964864	CD-472916	108.8015 -47.8181	3.480 ± 0.022	-9.652 ± 0.040	11.754 ± 0.040	-3										

and v_i :

$$r = \sqrt{v_b^2 + v_i^2} \quad (2)$$

$$\theta = \arctan\left(\frac{v_b}{v_i}\right) \quad (3)$$

$$v_0 = 0.044r \quad (4)$$

$$v_{rot} \sin(i) = \begin{cases} r + \frac{4v_0}{\pi} \theta, & \text{if } \theta \leq \frac{\pi}{4} \\ r - \frac{4v_0}{\pi} \theta + 2v_0, & \text{if } \theta > \frac{\pi}{4}, \end{cases} \quad (5)$$

where r is the standard rotational velocity and the applied broadening added in quadrature and v_0 is the empirically determined maximum deviation from addition in quadrature in polar coordinates. Orders for which the width falls below the derived broadening-width relation have their broadening interpolated on a quadratic fit to the relation. Orders that fail to interpolate a width are neglected. Most stars with rotation speed $< 100 \text{ km s}^{-1}$ utilize all 30 orders. The measured projected rotational velocity according to a given standard is the Doppler-uncertainty-weighted mean of the good orders' results. The uncertainty is the sample standard deviation of the good orders' results, added in quadrature with the standard's projected rotational velocity. Final projected rotational velocity $v_{rot} \sin(i)$ is the error weighted mean of the comparison standards' results. Final uncertainty is the greater of the error-weighted-mean error or, usually, the sample standard deviation of the comparison standards' results.

Testing this approach on our spectral standards with known projected rotational velocities, we find that we systematically overestimate the final $v_{rot} \sin(i)$ by $< 2 \text{ km s}^{-1}$ for $v_{rot} \sin(i) > 4 \text{ km s}^{-1}$, and our measurements are unreliable for $v_{rot} \sin(i) < 4 \text{ km s}^{-1}$ due to insufficient spectral resolution. All $v_{rot} \sin(i) < 4 \text{ km s}^{-1}$ are upper limits only. All $v_{rot} \sin(i) > 150 \text{ km s}^{-1}$ are lower limits only. Our method is most effective at measuring $v_{rot} \sin(i) > 2 \times$ the comparison standard's rotational velocity. Our catalogue of standards are amenable slow-rotating (see Appendix ??).

We successfully measure $v_{rot} \sin(i)$ values for 271 stars in the Gum Nebula, 18 of which have upper limits of 4 km s^{-1} , 33 of which have lower limits of 150 km s^{-1} . 116 stars are fast rotators with $v_{rot} \sin(i) \geq 40 \text{ km s}^{-1}$ (see Figure 6). Median uncertainty is 2.3 km s^{-1} , lower for slow rotators (median uncertainty 1.64 km s^{-1} for $v_{rot} \sin(i) < 40 \text{ km s}^{-1}$) and higher for fast rotators (median uncertainty 6.32 km s^{-1} for $v_{rot} \sin(i) \geq 40 \text{ km s}^{-1}$).

4.5. Li Equivalent Widths

To assess associations' youth, we measure equivalent widths (EW) of Li I $\lambda 6708$ (see Figure 5). We fit three

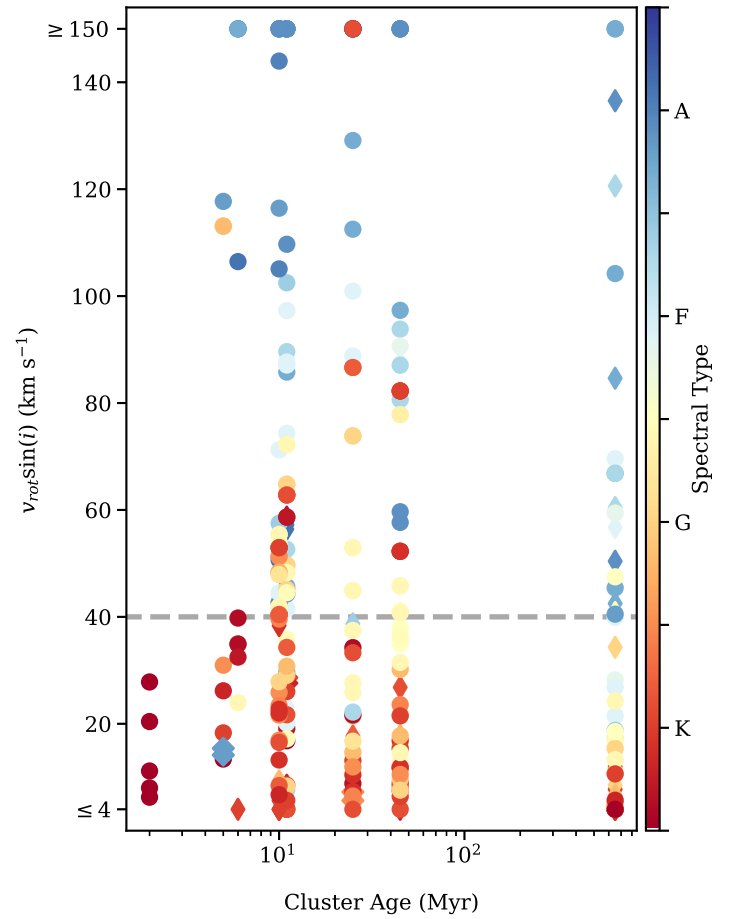


Figure 6. Projected rotational velocities $v_{rot} \sin(i)$ vs. ages. We have measured $v_{rot} \sin(i)$ for 271 association members based on CHIRON data and 5 members based on Keck I HIRES data (Yep & White 2020). Five of the 8 associations contain stars with $v_{rot} \sin(i) > 40 \text{ km s}^{-1}$. Circles are single-star association members. Diamonds are confirmed binaries (fat) or potential binaries (skinny). Twenty-seven cool stars later than type F5 are fast rotators.

Gaussians to the $6706 - 6710 \text{ \AA}$ region to account for the two lines of the lithium doublet at 6707.7635 \AA and 6707.9145 \AA and the blended iron line at 6707.4308 \AA (see Nisak et al. 2021). Equivalent width is calculated from the lithium components of the best-fit triple Gaussian. Uncertainties σ_{EW} are calculated as follows (Cayrel 1988; Deliyannis et al. 1993; Nisak et al. 2021):

$$\sigma_{EW} \approx \frac{\sqrt{fp}}{SNR}. \quad (6)$$

Here f is the full width at half maximum of the spectral line, p is the wavelength per pixel scale = 0.100 \AA at $\lambda 6708 \text{ \AA}$, and SNR is the signal-to-noise ratio per pixel in the spectral line. We measure values of Li EW from < 0.01 to 0.48 \AA , with median uncertainty 0.01 \AA . Values $< 0.01 \text{ \AA}$ are set to 0.01 \AA as an upper limit. We do

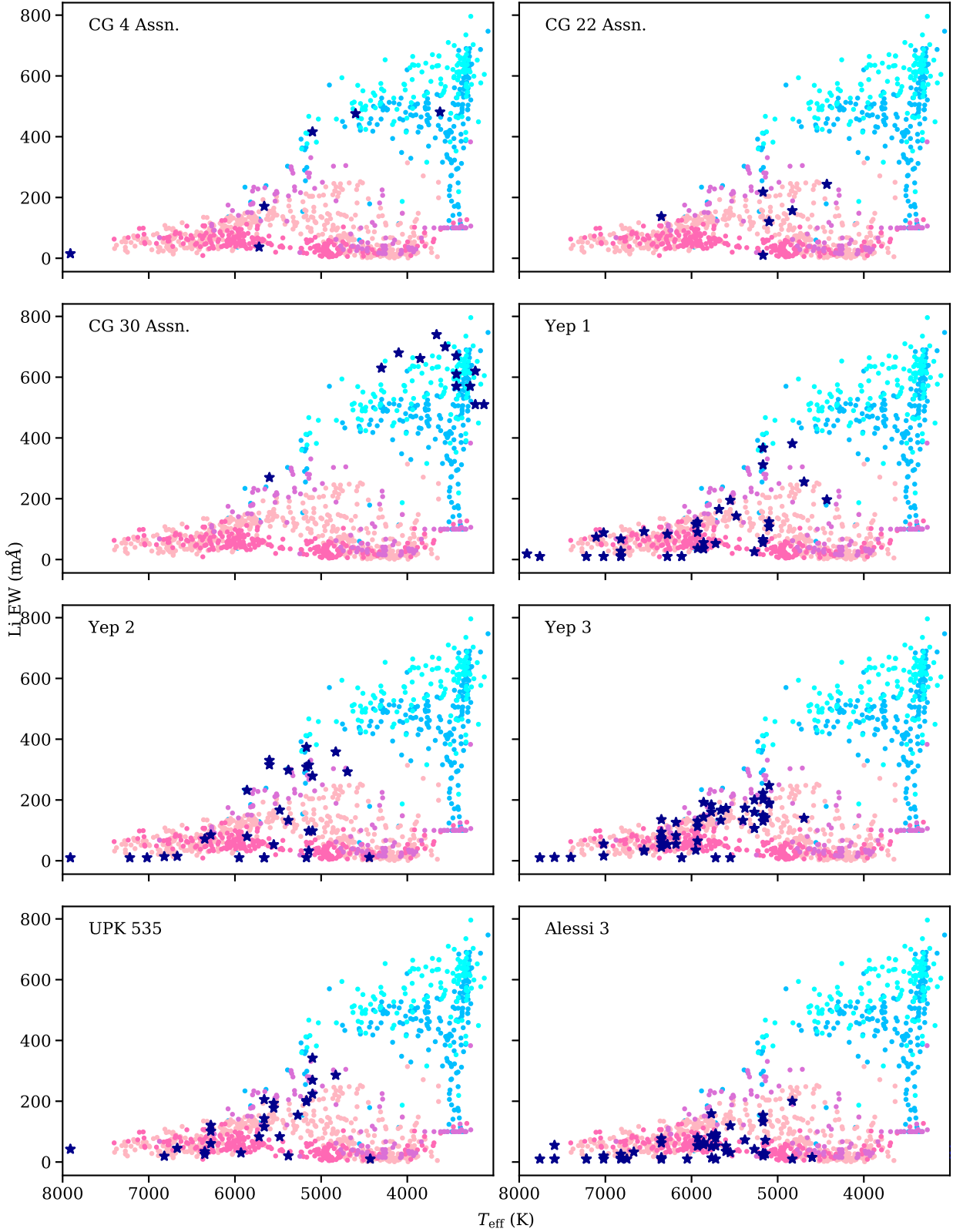


Figure 7. Li EW vs. T_{eff} . Light colored dots are from Gutiérrez Albarrán et al. (2020) and represent ages 1 – 3 Myr (cyan), 10 – 20 Myr (light blue), 34 – 41 Myr (lavender), 248 – 450 Myr (light pink), and 763 – 977 Myr (hot pink). Younger stars have stronger Li absorption, as do lower-mass stars. The associations in the Gum Nebula (dark blue stars) are fairly young, with ages 2 – 650 Myr. Their positions in Li EW vs. T_{eff} space are generally consistent with our isochrone age estimates.

not measure Li EW stars with $v_{rot} \sin(i) \geq 150 \text{ km s}^{-1}$. We do not correct Li EW for veiling, the continuum excess emitted by hot spots during stellar accretion, so the Li EW of stars in the youngest ($\lesssim 10 \text{ Myr}$) associations may be underestimated. Li EW for stars in the CG 30 Association are from Kim et al. (2005) and Yep & White (2020).

Lithium equivalent width (Li EW) provides a stellar age estimate independent from isochrone fits on a color-magnitude diagram. Lithium is destroyed via proton-helium reactions within a star's interior when temperatures reach $\sim 3 \cdot 10^6 \text{ K}$ (Bodenheimer 1965). Surface lithium is depleted in cool stars with outer convective zones over the course of 10 – 100 Myr (Jeffries et al. 2014). Because the rate of lithium depletion is spectral-type dependent (Randich et al. 1997; Jeffries et al. 2014; Gutiérrez Albarrán et al. 2020), we plot associations' Li EW vs. T_{eff} in Figure 7.

Comparisons with the lithium measurements of Gutiérrez Albarrán et al. (2020) provide empirical age ranges spanning from 1 Myr to 1 Gyr. The CG 4 and CG 30 associations have positions consistent with ages between 1 and 10 Myr (see Figure 7). Yep 1 and Yep 2 appear $< 34 \text{ Myr}$. UPK 535 is in the 34 – 41 Myr range. CG 22 and Yep 3 appear between 41 and 248 Myr. Alessi 3 appears older than 248 Myr but younger than 763 Myr.

Our approximate age ranges from Li EW vs. T_{eff} space are consistent with our isochrone-fit age estimates (see §3.9), with the exception of CG 22, whose isochrone-estimated age of 6^{+4}_{-2} Myr is significantly younger than its Li EW vs. T_{eff} age. Part of the discrepancy may be due to unmeasured veiling. Because of this and the probable connection between the CG 22 Association and its nearby star-forming cometary globule CG 22 (see §6.1), we defer to the isochrone-determined age.

4.6. $H\alpha$ Widths

Broad $H\alpha$ emission is associated with gas infall during accretion from a young star's circumstellar disk (Muze role et al. 1998). Narrow $H\alpha$ emission is associated with chromospheric activity, and $H\alpha$ absorption is simply from a star's photosphere. To measure $H\alpha \lambda 6562.81 \text{ \AA}$ emission or absorption, we first fit a Gaussian to the $6538 - 6588 \text{ \AA}$ region. We then integrate the normalized spectrum across the width of the Gaussian for which Gaussian flux < 0.99 for absorption or > 1.01 for emission. We choose to integrate the normalized spectrum because several of the $H\alpha$ features are broadened, saturated, or oddly shaped due to mixed absorption and emission (see Figure 8). Uncertainties are calculated as in Equation 6 with p set to 0.097 \AA at $\lambda 6562.81$

\AA . Twenty-eight spectra with low signal or mixed emission and absorption are measured manually and include additional uncertainty from visual inspection, added in quadrature to the σ_{EW} above. Our sample includes 36 stars with $H\alpha$ emission, 25 stars with mixed $H\alpha$ emission and absorption, and 224 stars with $H\alpha$ absorption. $H\alpha$ equivalent widths (EW) range from 4.46 \AA (absorption) to -32.29 \AA (emission; see Table 2). The median $H\alpha$ EW is 1.94 \AA (absorption), and the median uncertainty is 0.02 \AA . $H\alpha$ emitters appear in all 8 associations, even the older Alessi 3, but are more numerous in the younger associations.

For the 36 stars with $H\alpha$ emission and one star with mixed $H\alpha$ emission and absorption, we measure $H\alpha$ width at 10%-peak above the continuum, in km s^{-1} . Fast gas motions are associated with ongoing stellar accretion, whereas lower gas speeds are associated with chromospheric activity (White & Basri 2003; see §10). $H\alpha$ 10% widths range from 4 to 684 km s^{-1} . $H\alpha$ EW for stars in the CG 30 Association are from Kim et al. (2005) and Yep & White (2020), and their 10% widths are from Yep & White (2020).

4.7. Near-Infrared Excess

Hot dust in a young star's inner disk causes a near-infrared excess above the photosphere. We utilize the dwarf colors of Pecaut & Mamajek (2013) to measure infrared excess in $J - K$ color. We cross-match our association membership lists with 2MASS using CDS X-Match (Skrutskie et al. 2006; Boch et al. 2012). We then compare all apparent $J - K$ colors with stars' intrinsic $J - K$ colors based on their spectral types. We only measure color excesses for spectroscopically observed stars. Association-averaged results range from 0.024 to 0.311 mag and generally decrease with increasing association age (see Figure 9 and Table 3)).

Near-infrared excess is associated with a strong signal of accretion called spectral veiling, a filling-in of spectral lines and bluing of color (White & Ghez 2001). We see this effect in several spectra but have not measured it.

4.8. Exceptions

In measuring the radial velocity of the double-line spectroscopic binary star CD-46 3194, each of the two cross-correlation peaks are measured separately. We assume both stars have the same mass and therefore average their radial velocities to derive a systemic velocity of $7.1 \pm 1.7 \text{ km s}^{-1}$. In measuring rotational velocity, each of the two cross-correlation peaks of the binary star CD-46 3194 are again measured separately. One component has $v_{rot} \sin(i) = 15.4 \pm 3.4 \text{ km s}^{-1}$, and the component has $v_{rot} \sin(i) = 14.2 \pm 4.0 \text{ km s}^{-1}$.

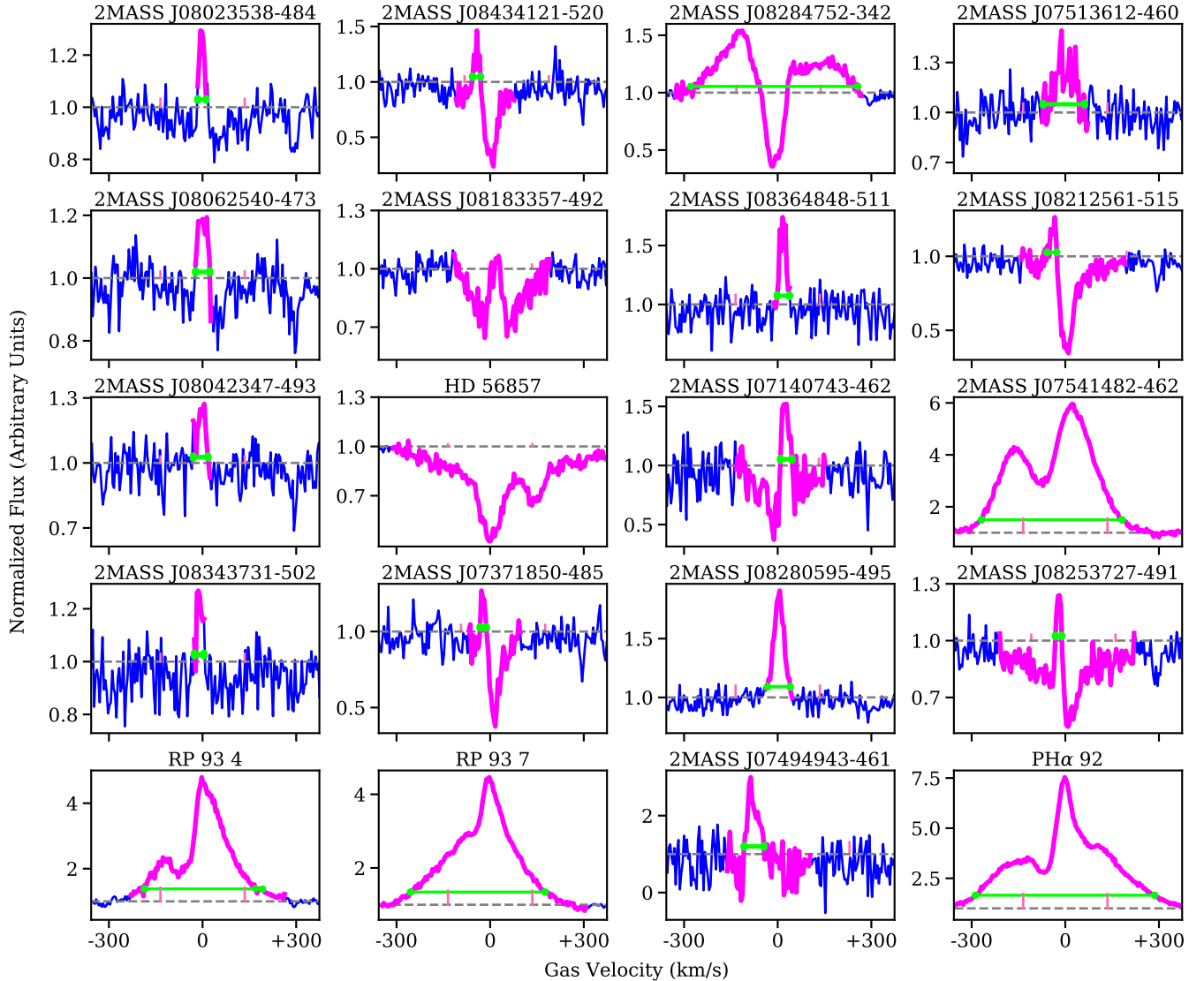


Figure 8. Sample of H α profiles with emission or mixed emission and absorption, in normalized flux vs. gas velocity. Equivalent width is calculated over the magenta portion. Lime green marks the H α 10% width for emitters. Pink vertical lines up through the 10% width indicate a gas motion spread of 270 km s $^{-1}$, our empirical boundary between accreting and nonaccreting stars.

The spectrum of the candidate double-line spectroscopic binary 2MASS J08443526-5234117 does not manifest double cross-correlation peaks, perhaps because its SNR is too low or because the star is not a spectroscopic binary (see §4.2). We treat 2MASS J08443526-5234117 like a single star when measuring its radial and rotational velocity.

The lithium feature CD-46 3194 cannot be resolved into two separate lines, so both components are measured together. Thus Li EW for CD-46 3194 is an upper limit. The H α feature of CD-46 3194 also could not be resolved into two separate lines, so both components are measured together. Thus H α EW for CD-46 3194 is also an upper limit.

5. ASSOCIATION PROPERTIES

We determine the ensemble association v_r , $E(BP - RP)_{\text{assn}}$, and A_G by taking the error-weighted mean of associations' member star measurements (see §4.2, and §4.3). We give our prescription for verifying association members and determine association age and total mass. Association properties are assembled in Table 4.

5.1. Association Verification

Our initial star selection process was relatively narrow (see 2), so chance of association membership is high. Nonetheless, we calculate each star's z-score relative to its association's mean in RA , Dec , d , μ_α , μ_δ , and, where available, v_r and Li EW. Stars with a high z-score in a couple parameters (e.g. stars towards the edge of the

Table 3. Sample of Stellar Properties of Spectroscopically Observed Stars

Star Name	Spectral Epoch	Type	Class	v_r Uncert. (km s $^{-1}$)	$v_{\text{rot}} \sin(i)$ (km s $^{-1}$)	Binary Flag	H α EW (Å)	H α 10% W (km s $^{-1}$)	Li EW (Å)	Infrared Excess (mag)	Assn. Name
RP93 7	1	K4V	1.0	22.47 ± 0.42	26.2 ± 1.6	-	-14.642 ± 0.017	431 ± 12	0.476 ± 0.026	0.477 ± 0.062	CG 4 Assn.
PH α 92	1	K3V	1.0	20.09 ± 0.92	32.5 ± 1.9	-	-32.293 ± 0.012	575 ± 12	0.157 ± 0.016	0.933 ± 0.075	CG 22 Assn.
TYC 8134-2633-1	1	F7V	1.0	23.01 ± 0.87	48.3 ± 3.0	-	2.196 ± 0.020	...	0.000 ± 0.022	0.023 ± 0.037	Yep 1
HD 70977	1	A9V	2.0	19.3 ± 2.0	87.1 ± 3.1	-	3.825 ± 0.018	...	0.0112 ± 0.0044	0.022 ± 0.049	Yep 3
CD-46 3075	1	A7V	1.0	-10.1 ± 6.6	121 ± 15	SB1?	3.364 ± 0.014	...	0.0000 ± 0.0085	0.091 ± 0.035	Alessi 3

NOTE— Full table is available in online resources.

Table 4. Association Properties

Association Name	No. Stars	Age (Myr)	$E(BP - RP)_{\text{assn}}$ [Fe/H]	$E(BP - RP)_{\text{assn}}$ (mag)	A_G (mag)	Infrared Excess (mag)	M_{tot} (M_{\odot})	v_r (km s $^{-1}$)	Accretion Fraction (%)	G_0
CG 4 Assn.	34	5^{+5}_{-2}	0.1	0.349 ± 0.028	0.698 ± 0.056	0.311 ± 0.037	30.8 ± 3.1	21.6 ± 1.1	29 ± 20.	$2.1^{+7.2}_{-1.2}$
CG 22 Assn.	102	6^{+4}_{-2}	0.1	0.223 ± 0.077	0.45 ± 0.15	0.109 ± 0.045	77.0 ± 9.4	22.2 ± 1.9	18 ± 13	$3.61^{+0.87}_{-2.0}$
CG 30 Assn.	29	$2.0^{+2.0}_{-1.5}$	0.1	0.04 ± 0.14	0.08 ± 0.29	0.245 ± 0.065	20.8 ± 2.7	22.8 ± 2.0	29 ± 14	$6.6^{+3.2}_{-2.7}$
Yep 1	534	11^{+9}_{-4}	0.2	0.134 ± 0.055	0.27 ± 0.11	0.062 ± 0.031	398 ± 56	21.4 ± 1.8	1.6 ± 1.6	$6^{+19}_{-4.5}$
Yep 2	443	10^{+5}_{-4}	0.0	0.161 ± 0.054	0.32 ± 0.11	0.068 ± 0.034	327 ± 50.	20.8 ± 1.4	2.3 ± 2.3	$3^{+30.}_{-1.8}$
Yep 3	297	45^{+55}_{-20}	0.2	0.036 ± 0.027	0.072 ± 0.053	0.024 ± 0.022	252 ± 27	19.4 ± 1.6	0.0 ± 0.0	$7.8^{+2.0}_{-4.6}$
UPK 535	174	25^{+15}_{-10}	0.1	0.059 ± 0.022	0.120 ± 0.043	0.053 ± 0.016	145 ± 13	10.1 ± 1.6	0.0 ± 0.0	$11.2^{+9.4}_{-8.0}$
Alessi 3	260	650^{+100}_{-400}	0.2	0.037 ± 0.044	0.075 ± 0.088	0.039 ± 0.034	300. ± 26	0.2 ± 1.1	0.0 ± 0.0	$3.4^{+2.7}_{-2.1}$

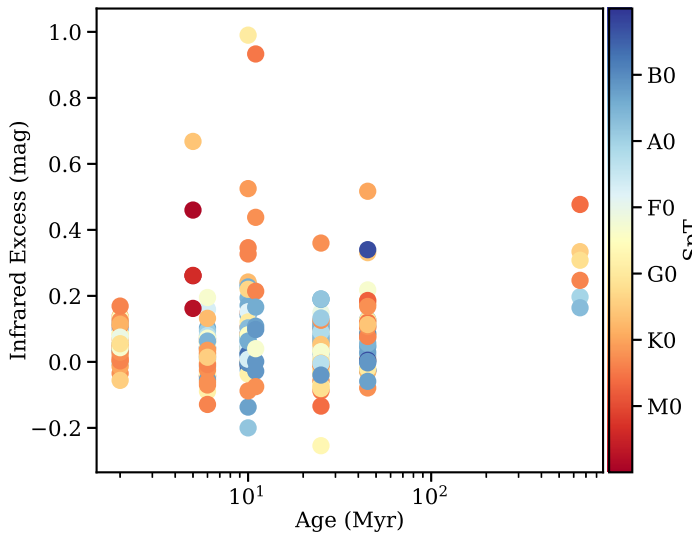


Figure 9. Infrared excess in $J - K$ vs. age. The dust in young stars' accretion disks or a debris disks tend to cause infrared excess. We calculate infrared excess by comparing stars' apparent $J - K$ colors with their intrinsic colors according to their spectral types and the dwarf colors of (Pecaut & Mamajek 2013).

association) may still be members, but stars with a high z-score in several parameters may not be. We therefore calculate an average absolute-value z-score and inspect any stars that score higher than 2. One star in Yep 1, two stars in Yep 2, and three stars in Theia 120 are deemed nonmembers and discarded. All six nonmembers are dimmer than $V = 13.5$ mag.

5.2. Total Stellar Masses

Total stellar mass of each association is calculated by summing individual stellar masses, the estimated mass of undiscovered cool stars according to an initial mass function (IMF), and estimated unresolved binary companion masses for a total binarity of 50 per cent. Uncertainties are worst-case uncertainties, summed directly.

Our samples extend down to apparent $G \sim 20$ mag and are reasonably complete down to $\sim 0.2 M_{\odot}$, or spectral type \sim M4V. According to the IMF of Kroupa (2001), 48% of stars are M-type stars and contribute 28% of the total association mass, and 38% are brown dwarfs that contribute 4.3% of the total association mass. Counting all stars up to each association's largest stellar mass, we calculate that we are missing anywhere from 9 to 42% of the mass of each association, median 20%, with an assigned uncertainty of 20% of the missing amount to account for uncertainties in choice of IMF and the edge of our samples' spectral type completeness.

To account for binary companions when summing stellar masses, we double the mass of double-line binary stars, and we approximate each confirmed or suspected single-line binary star's companion mass as half the mass of the primary (see §4.3 for binary criteria). Known-companion mass adds 2 to 22% of the single-star mass to the total mass, median 9% of the total single-star mass. If the associations have 50 per cent binarity and companion stars each possess half the mass of their primaries, randomly assigned unresolved binarity over 10,000 ran-

domized trials adds mass equaling 20 – 24% of the total single-star mass, median 22%.

Summing all masses and uncertainties within each association, association total stellar masses M_{tot} span 21 – 398 M_{\odot} (see Table 4), with a median worst-case uncertainty (all component uncertainties summed directly) of 11% of total stellar mass. This is again statistical uncertainty, with systematic uncertainty likely higher.

6. DISCUSSION

6.1. Star Formation Associated with Cometary Globules

As described in §2, the associations were first identified by searching for stellar associations in close proximity to cometary globules in the Gum Nebula. However, the identified associations may or may not be physically associated with these ongoing sites of isolated star formation. Here we examine all 8 associations for connections with their nearby cometary globules. We consider the cometary globules we invoked when searching for the found associations as well as six additional cometary globules and dark clouds that have measured radial velocities (see Figures 3 and 1).

A cometary globule's connection with a stellar association gives us a way to estimate a first distance to that globule, a typically difficult quantity to measure for diffuse clouds.

6.1.1. CG 4 Association and CG 4

The CG 4 Association is sparse and young, 5^{+5}_{-2} Myr. Of all 7 new associations in this paper, the association by CG 4 most closely resembles the CG 30 Association in its sparseness and its core's proximity to a globule actively forming stars (Reipurth & Pettersson 1993; Pettersson 2007; Kim et al. 2005; Yep & White 2020). CG 4 is spatially within the CG 4 Association, 0.24° from the center. CG 6 is also spatially very near the association (Reipurth & Pettersson 1993; Kim et al. 2006), about 0.55° from the center. CGs 4 and 6 have radial velocities $19.0 \pm 1.2 \text{ km s}^{-1}$ and $18.2 \pm 1.1 \text{ km s}^{-1}$, respectively (Sridharan 1992), and the association has a median velocity of $21.6 \pm 1.1 \text{ km s}^{-1}$, so their connection with the CG 4 Association is plausible. We therefore estimate the distances to CG 4 and CG 6 are the association's error-weighted-mean distance of $415.8 \pm 1.0 \text{ pc}$. This puts CG 4 and CG 6 about 1.8 pc and 4.0 pc from the center of the CG 4 Association, respectively.

6.1.2. CG 22 Association and CG 22

CG 22 is 1.18° from the center of the CG 22. Choudhury & Bhatt (2009) deduced CG 22's motion from the young star PH α 92 within it. Following Choudhury and

Bhatt's example, we can infer that CG 22's v_r is $20.09 \pm 0.92 \text{ km s}^{-1}$. The CG 22 Association's error-weighted-mean v_r is similar, $22.2 \pm 1.9 \text{ km s}^{-1}$, and the association's proper motions match PH α 92's. Considering CG 22's young age (6^{+4}_{-2} Myr) and ongoing star formation in its bright-rimmed head, CG 22 is likely associated with the CG 22 Association. We therefore estimate the distance to CG 22 is the association's error-weighted-mean distance of $355.06 \pm 0.54 \text{ pc}$. This puts CG 22 about 7.3 pc from the center of the CG 22 Association.

6.1.3. CG 30 Association and CG 30

CG 30 is spatially within the CG 30 Association, 0.31° from the center. The CG 30 Association is very young ($2.0^{+2.0}_{-1.5}$ Myr) and moves at $v_r = 22.8 \pm 2.0 \text{ km s}^{-1}$, consistent with the cometary globule's $v_r = 22.8 \text{ km s}^{-1}$). Two other cometary globules in the vicinity, CG 31 and CG 38, have radial velocities $23.3 - 24.2 \text{ km s}^{-1}$ and $20.3 \pm 1.2 \text{ km s}^{-1}$, respectively, that are also consistent with the association's. The association and the CG 30-31-38 cometary globule are dynamically connected (Kim et al. 2005; Yep & White 2020). We therefore estimate the distance to the CG 30-31-38 cometary globule complex is the association's error-weighted-mean distance of $356.6 \pm 1.4 \text{ pc}$. This puts CG 30 about 1.9 pc from the center of the CG 30 Association.

6.1.4. Yep 1 and CG 3

Yep 1 is populous (535 stars), large, round, and fairly young, 11^{+9}_{-4} Myr. The radial velocity of CG 3 is $17.4 \pm 1.0 \text{ km s}^{-1}$ (Sridharan 1992), whereas the median radial velocity of the association is $21.4 \pm 1.8 \text{ km s}^{-1}$. With a 3.9 km s^{-1} discrepancy in radial velocity and a 2.32° separation between CG 3 and the association center (would be 15.9 pc at Yep 1's distance), connection with the globule is possible but unlikely.

6.1.5. Yep 2 and CG 14

The globule CG 14 is beyond the edge of the association, 3.91° from the association's core (would be 27.5 pc at Yep 2's distance). The radial velocity of CG 14 is $16.4 \pm 1.0 \text{ km s}^{-1}$ (Sridharan 1992), while the median radial velocity of Yep 2 is $20.9 \pm 1.5 \text{ km s}^{-1}$. Though the association is young, 10^{+5}_{-4} Myr, it may not be physically connected with the cometary globule CG 14.

6.1.6. Yep 3 and CG 17

The cometary globule CG 17 is 2.06° from the median center position of 45-Myr-old Yep 3 (would be 12.2 at Yep 3's distance) and moving at a radial velocity of $19.3 \pm 0.4 \text{ km s}^{-1}$. The association has a very similar median radial velocity of $19.4 \pm 1.6 \text{ km s}^{-1}$. Despite the similar kinematics, Yep 3's age of 45^{+55}_{-20} Myr is well past

when most clusters lose their molecular cloud material (Krumholz et al. 2019; ?). Therefore we assume Yep 3 and CG 17 are not connected.

6.1.7. UPK 535 and GDC 1

GDC 1 is spatially within UPK 535 and moving at a radial velocity of $22.6 \pm 1.2 \text{ km s}^{-1}$. Its proper motions are unknown. UPK 535 is about 22 Myr old, has a median radial velocity of $10.1 \pm 1.6 \text{ km s}^{-1}$, and is not associated with GDC 1.

UPK 535 has a drawn-out shape much like Yep 3 and in fact partially overlaps it. The two associations have recently collided. See Yep & White (2021) for a full analysis.

6.1.8. Alessi 3 and CG 1

Though CG 1 is within our search radius for Alessi 3, it is unlikely they are associated. Alessi 3 is an older open association, 500 Myr according to Alessi et al. (2003) and 650^{+100}_{-400} Myr according to our own analysis (see §§4.5 & 5). An association of this age is unlikely to be associated with the new star formation at CG 1. Additionally, the proper motions and radial velocities of Alessi 3 and CG 1 differ ($\mu_\alpha = -9.81 \pm 0.16$ vs. -4.2 ± 0.2 mas yr^{-1} , $\mu_\delta = 11.85 \pm 0.17$ vs. 6.1 ± 1.9 mas yr^{-1} , and $v_r = 0.2 \pm 1.1$ vs. $20.6 \pm 1.4 \text{ km s}^{-1}$, respectively (Sridharan 1992; Alessi et al. 2003; Choudhury & Bhatt 2009; see §4.3).

Because CG 1 is associated with star formation, hosting Berries 135 = NX Pup A in its head (Reipurth 1983; Pettersson 2007), another association search in the vicinity of CG 1 may be worthwhile.

6.2. Gum Nebula Radiation Environment

The FUV radiation output of ζ Pup, γ^2 Vel, the Vela XYZ progenitor, and the Vela OB2 association can be calculated throughout the Gum Nebula as G_0 , the ratio of a region's FUV radiation compared to average interstellar $G_{0,ISM} = 1.6 \times 10^3 \text{ ergs s}^{-1} \text{ cm}^{-2}$ (Habing 1968; Winter et al. 2018). We calculate G_0 from integrating Kurucz stellar models for ζ Pup, γ^2 Vel, the Vela XYZ progenitor, and stars of the Vela OB2 association at each association's distance from each of these stars (see appendix of Yep & White 2020). G_0 ranges from 2.1 to 11.2, with median 4.8. These G_0 values and the presence of cometary globules and O-type stars lead us to designate the Gum Nebula a moderate radiation environment.

The presence of B-type stars within some associations may locally raise G_0 by 1 – 10 points, but we do not at present take this into account. Ideally we would include each association's B-type stars to map local G_0 . We

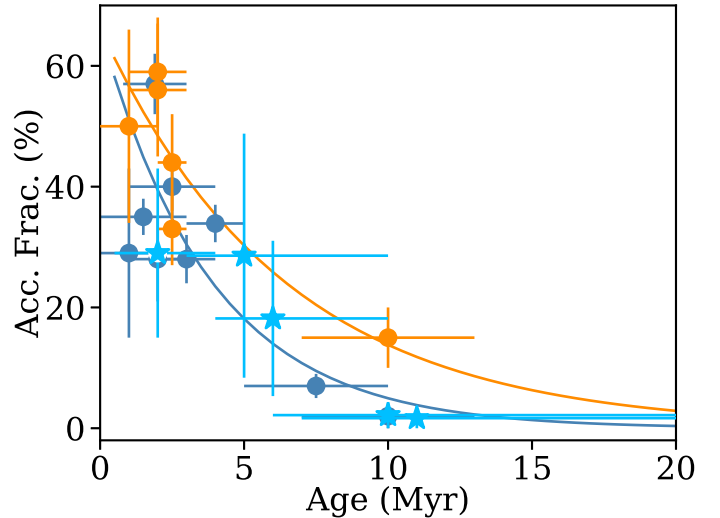


Figure 10. Association accretor fraction vs. association age. Quiescent-region associations (orange circles) tend to have higher accretor fractions per age than external-radiation-region associations (steel blue circles). Gum Nebula associations' accretor fractions (blue stars) appear more consistent with the external-radiation-region trend.

could then check if disk loss is more due to local B-type stars or the O-type stars powering the Gum Nebula.

We gather comparison clusters and associations from Mohanty et al. (2005) and Yep & White (2020). We categorize these comparison clusters and associations as *irradiated* if cometary globules or OB associations are present and as *quiescent* if no cometary globules or OB associations are present. This categorization is preliminary. Ideally we would determine an averaged G_0 cutoff between irradiated and quiescent clusters, but G_0 has never been calculated for most of our comparison clusters and associations. Additionally, some of the youngest clusters are embedded, which may shield some of their young stars from radiation in complex ways. A detailed, consistent calculation of G_0 for all our target-and comparison clusters and associations is in order, but that is beyond the scope of this paper.

6.3. Photoevaporated Protoplanetary Disks

Young stars possess dusty, gaseous accretion disks for the first few million years of their lives, until stellar winds or the pressure of their own radiation dispels them. The fraction of stars in an association that are still accreting, N_{acc}/N_{tot} , thus decreases over time. In a quiescent star-forming region free of massive stars, such as Tau-Aur, $N_{acc}/N_{tot} = 30 – 50\%$ is normal for age 1 – 5 Myr, and $N_{acc}/N_{tot} = 15 – 30\%$ is normal for age 5 – 10 Myr (Mohanty et al. 2005; Yep & White 2020). In an irradiated region that is inhabited by an O-type star or several B-type stars, $N_{acc}/N_{tot} = 10 – 30\%$ is normal

for age 1 – 5 Myr, and $N_{acc}/N_{tot} = 1 – 10\%$ is normal for age 5 – 10 Myr (Yep & White 2020).

White & Basri (2003) demonstrate that $W_{10}(\text{H}\alpha) > 270 \text{ km s}^{-1}$ is associated with accretion. This easy-to-measure indicator is less sensitive to stellar mass than H α EW and optical veiling (White & Basri 2003; Adams et al. 2004), and potentially affected only slightly by circumstellar disk inclination. Based on the number of accretors in each association divided by the number of stars in each association, we calculate each association’s accretor fraction N_{acc}/N_{tot} , the fraction of stars that still have their accretion disks.

None of the three older associations (>11 Myr) have any stars that are accreting. All five young associations (1 – 11 Myr) within the Gum Nebula exhibit low accretor fractions for their ages, 0 – 29% for ages 2 – 11 Myr. To illustrate this, we plot the accretor fractions vs. ages of quiescent and irradiated regions in Figure 10, using data from Mohanty et al. (2005) and Yep & White (2020). We then fit a power law to the quiescent regions and another power law to the irradiated regions. The accretor fractions of the five young clusters in the Gum Nebula appear more consistent with the irradiated environments than the quiescent environments. This finding, however, relies on our preliminary distinction between irradiated and quiescent environments, and on inhomogeneous methods for distinguishing accretors from nonaccretors across the several studies synthesized in (Yep & White 2020). In addition to calculation of average and local G_0 , a consistent, improved designation of accretors vs. nonaccretors in all target- and comparison associations and clusters will yield more robust results.

6.4. High Rotational Velocities for Age

Fast rotation of cool (FGK-type) stars, along with Li abundance and chromospheric activity (itself correlated with fast rotation), is associated with youth (Cutispoto et al. 2002). Because a cool star’s interaction with its own protoplanetary disk could magnetically brake the star’s rotation, cool-star fast rotation for age could be a sign of early disk dispersal. Across the eight associations, 27 cool stars earlier than type F5 have projected rotational velocity $v_{rot} \sin(i) > 40 \text{ km s}^{-1}$ (see Figure 6). Three cool stars (CD-46 3212, 2MASS J08292220-5050369, 2MASS J08351629-5156166) are extraordinarily fast, with $v_{rot} \sin(i) > 100 \text{ km s}^{-1}$. The fastest, K2V-type star 2MASS J08292220-5050369, is rotating at $>150 \pm 20 \text{ km s}^{-1}$. However, without a comparison sample of $v_{rot} \sin(i)$ values in quiescent regions, we cannot use projected rotation speeds to indirectly probe early disk dispersal.

6.5. Characteristics of Cometary Globule Associations

The three clusters most likely associated with their nearby cometary globules are the CG 4, CG 22, and CG 30 Associations (Kim et al. 2005; Pettersson 2007; Yep & White 2020). All three globules are actively forming stars (Reipurth & Pettersson 1993; Kim et al. 2006; Rebull et al. 2011; Yep & White 2020). All three are also fairly sparse, each association comprising $\lesssim 100$ stars, and the structures of the CG 4 and CG 30 Associations are filamentary. The CG 4, CG 22, and CG 30 Associations’ sparseness is consistent with the suggestion that cometary globules produce isolated, low-mass stars (Bhatt 1993; Kim et al. 2005; Walch et al. 2013), due to external radiation spurring relatively low-mass globules to form stars (Bhatt 1993; Maheswar & Bhatt 2008). The highest-mass stars in the CG 4, CG 22, and CG 30 Associations are 1.86, 2.75, and $0.97 M_\odot$, respectively. CG 4 and CG 30 have no stars $> 2 M_\odot$, while CG 22 has 5 such stars.

External radiation from the hot bright O-type stars at the Gum Nebula’s heart may limit Gum Nebula young stars’ ability to form planets. Far-ultraviolet radiation erodes protoplanetary disks early in even moderate-radiation environments ($G_0 = 2.1 – 7.8$ for the five young clusters; see Table 4 and Figure 10). Far-ultraviolet radiation may also damage or destroy the ingredients necessary to planet formation (Sabbi et al. 2020). These factors could result in a lower number of planets around stars in the Gum Nebula and other hot-star-irradiated regions.

7. SUMMARY

The Gum Nebula is home to hot stars, cometary globules, and several young associations and is thus an ideal location to study effects of external radiation on star formation and young stars’ planet-forming disks. From spectroscopic observations of 284 stars in seven of the 8 young associations we here study throughout the Gum Nebula, combined with *Gaia* DR2 data, we conclude the following:

- We develop an empirical method Cluster Finder for finding clusters and associations in *Gaia* DR2 data. Using this method, we find 8 young associations in the Gum Nebula.
- We present a catalogue of 81 high-quality spectral standards observed with CHIRON in fiber mode, spanning from spectral type O9.5V to M5.5V.
- We observe 284 stars in 7 of the 8 associations in the Gum Nebula.

- From spectra and *Gaia* DR2 data, we derive stellar and association properties.
- Five of the 8 associations we study in the Gum Nebula, including the CG 30 Association, are young (≤ 10 Myr), based on lithium abundances and isochrone fits.
- Stars exhibiting H α emission are present in all 8 associations. Stars with strong H α emission indicative of ongoing accretion are present in the five young associations.
- All five young associations exhibit low accretor fractions (0 – 29%) for their ages (2 – 11 Myr), possibly due to the Gum Nebula's moderate radiation environment ($G_0 = 2.1 - 7.8$) eroding young stars' protoplanetary disks. Such external radiation may thus shorten Gum Nebula stars' timescales for forming planets, damage or destroy planet-forming ingredients, and reduce Gum Nebula stars' abilities to form planets.
- Three of the 8 associations (CG 4, 22, and 30 Associations) are likely associated with their nearby

cometary globules. These associations are relatively sparse, and two have filamentary structure.

- Based on cometary globules' connections with their nearby stellar associations, we estimate first distances to several cometary globules: CG 4 and CG 6 are 415.4 ± 1.0 pc away, CG 22 is 355.06 ± 0.54 pc away, and CG 30, CG 31, and CG 38 are 356.6 ± 1.4 pc away.

Young stars in the Gum Nebula exist in a moderate radiation environment and, due to external ionizing radiation from their massive neighbors, may lose their protoplanetary disks early.

A big thanks to my lovely boyfriend R. C. Marks! A double-thanks to A. Nisak, who provided initial codes for measuring radial velocity, rotational velocity, and elemental abundances. A big thanks to A. Nisak, H. James, L. Paredes, and W.-C. Jao aiding with the scheduling of my targets on CHIRON and reducing my spectra, and to T. Henry for granting internal telescope time.

Software: Python, Jupyter Notebook, IDL, IRAF

REFERENCES

- Adams, F. C., Hollenbach, D., Laughlin, G., et al. 2004, ApJ, 611, 360
- Alessi, B. S., A. Moitinho, & W. S. Dias. 2003, A&A 410, 565
- Ammler-von Eiff, M., & A. Reiners. 2012, A&A, 542, 116
- Andrae, R., M. Fouesneau, O. Creevey, et al. 2018, A&A, 616, A8
- Apellániz, M., J., E. J. Alfaro, & A. Sota. 2008, arXiv, 0804.2553v1
- Asensio-Torres, R., Currie, T., Janson, M., et al. 2019, A&A, 622, A42
- Bailer-Jones, C. A. L., Rybizki, J., Fouesneau, M., Mantelet, G., & Andrae, R. 2018, AJ, 156, 58
- Baraffe, I., D. Homeier, F. Allard, & G. Chabrier. 2015, A&A, 577, A42
- Basri, G., E. L. Martín, & C. Bertout. 1991, A&A, 252, 625B
- Bate, M. R., I. A. Bonnell, & V. Bromm. 2003, MNRAS, 339, 577
- Beasor, E. R., Davies, B., Smith, N., et al. 2019, MNRAS, 486, 266
- Bertoldi, F. 1989, ApJ, 346, 735
- Beuermann, C. P. 1973, Ap&SS, 20, 27
- Bhatt, H. C. 1993, MNRAS, 262, 812B
- Boch, T., Pineau, F., & Derriere, S. 2012, Astronomical Data Analysis Software and Systems XXI, 461, 291
- Bodenheimer, P. 1965, ApJ, 142, 451B
- Bouvier, J., S. P. Matt, S. Mohanty, et al. 2014, arXiv, 1309.7851v1
- Brandt, J. C., T. P. Stetzer, D. L. Crawford, & S. P. Maran. 1971, ApJ, 163, 99
- Bronfman, L., L. A. Nyman, & J. May. 1996, A&A, 115, 81
- Bronfman, L., L. A. Nyman, & J. May. 1992, A&A, 265, 577L
- Butler, R. P., G. W. Marcy, E. Williams, et al. 1996, PASP, 108, 500
- Cantat-Gaudin, T., Jordi, C., Vallenari, A., et al. 2018, A&A, 618, A93
- Cantat-Gaudin, T., C. Jordi, N. J. Wright, et al. 2019, A&A, 626, 17
- Cantat-Gaudin, T., & F. Anders. 2020, A&A, 633, 99
- Caraveo, P.A., A. De Luca, R. P. Mignani, & G. F. Bignami. 2001, ApJ, 561, 930
- Cayrel, R. 1988, IAUS, 132, 345
- Cha, A. N., K. R. Sembach, & A. C. Danks. 1999, ApJ, 515L, 25C
- Choi, J., A. Dotter, C. Conroy, et al. 2016, ApJ, 823, 102
- Cochran, W. D. 1988, ApJ, 334, 349C

- Choudhury, R., & H. C. Bhatt. 2009, MNRAS, 393, 959
- Cutispoto, G., L. Pastori, L. Pasquini, et al. 2002, A&A 384, 491
- Czesla, S., S. Schröter S., C. P. Schneider, et al. 2019, PyA: Python astronomy-related packages (ascl:1906.010)
- Delfosse, X., T. Forveille, C. Perrier, & M. Mayor. 1998, A&A, 331, 581
- Deliyannis, C. P., Pinsonneault, M. H., & Duncan, D. K. 1993, ApJ, 414, 740
- De Medeiros, J. R., S. Alves, S. Udry, et al. 2014, A&A, 561, 126
- Desidera, S., E. Covino, S. Messina, et al. 2015, A&A, 573, 126
- Dias, W. S., B. S. Alessi, A. Moitinho, & J. R. D. Lépine. 2002, A&A, 389, 871
- Díaz, C. G., J. F. González, H. Levato, & M. Grosso. 2011, A&A, 531, 143
- Dotter, A. 2016, ApJS, 222, 8
- Elmegreen, B. G. 2011, arXiv, 1101.3112
- Evans, D. W., M. Riella, F. De Angeli, et al. 2018, A&A 616, 4
- Franciosini, E., G. G. Sacco, R. D. Jeffries, et al. 2018, arXiv, 1807.03621v1
- Gaia Collaboration, Prusti, T., de Bruijne, J. H. J., et al. 2016, A&A, 595, A1
- Gaia Collaboration, Brown, A. G. A., Vallenari, A., et al. 2018, A&A, 616, A1
- Gallet, F., & J. Bouvier. 2013, A&A, 556, 36
- Gontcharov, G. A. 2006, AstL, 32, 759
- Gray, D. 1992, *The Observation and Analysis of Stellar Photospheres*, Cambridge: Cambridge Univ. Press
- Gum, C. S. 1952, Observatory, 72, 151
- Gutiérrez Albarrán, M. L., D. Montes, M. Gómez Garrido, et al. 2020, A&A 643, 71
- Habing, H. J. 1968, BAN, 19, 421
- Hartigan, P., L. Hartmann, S. J. Kenyon, R. Hewett, & J. Stauffer. 1989, ApJS, 70, 899
- Hartigan, P., S. J. Kenyon, L. Hartmann, et al. 1991, ApJ, 382, 617H
- Hartmann, L., G. Herczeg, & N. Calvet. 2016, ARA&A, 54, 135
- Herczeg, G. J. & Hillenbrand, L. A. 2015, ApJ, 808, 23
- Hillenbrand, L. A. 1997, AJ, 113, 1733H
- Hillenbrand, L. A., A. Bauermeister, & R. J. White. 2008, in ASP Conf. Ser., Cool Stars 14, ed. G. van Belle (San Francisco: ASP), in press (astro-ph/0703642)
- Jao, W.-C., T. J. Henry, D. R. Gies, & N. C. Hambley. 2018, ApJ, 861, 11
- Jeffries, R. D., R. J. Jackson, M. Cottaar, et al. 2014, A&A, 563, A94
- Kajdič, P., B. Reipurth, A. C. Raga, & J. Walawender. 2010, RMAA, 46, 67
- Kharchenko, N. V., R.-D. Scholz, A. E. Piskunov, S. Röser, E. Schilbach. 2007, AN, 328, 889
- Kim, J. S., Walter, F. M., Wolk, S. J., et al. 2006, American Astronomical Society Meeting Abstracts
- Kim, J. S., F. M. Walter, & S. J. Wolk. 2005, ApJ, 129, 1564
- Kim, K. H., D. M. Watson, P. Manoj, et al. 2016, ApJ, 226, 8
- Kounkel, M. & Covey, K. 2019, AJ, 158, 122
- Kroupa, P. 2001, MNRAS, 322, 231
- Krumholz, M. R., McKee, C. F., & Bland-Hawthorn, J. 2019, ARA&A, 57, 227
- Kuhn, M. A., Hillenbrand, L. A., Sills, A., et al. 2019, ApJ, 870, 32
- Lada, J. C., & E. A. Lada. 2003, ARA&A, 41, 57
- Leahy, D. A., J. Nousek, & G. Garmire. 1992, ApJ, 385, 561
- Magazzú, A., R. Rebolo, & Y. V. Pavlenko. 1992, ApJ, 392, 159M
- Maheswar, G., & H. C. Bhatt. 2008, ASS, 315, 215
- Maldonado, J., R. M. Martínez-Arnáiz, C. Eiroa, D. Montes, & B. Montesinos. 2010, A&A, 521, 12
- Martínez-Arnáiz, C., J. Maldonado, D. Montes, C. Eiroa, & B. Montesinos. 2010, A&A, 520, 79
- Marsden, S. C., P. Petit, S. V. Jeffers, et al. 2014, MNRAS, 444, 3517
- Martín, E. L., R. Rebolo, A. Magazzú, & Y. V. Pavlenko. 1994, A&A, 282, 503M
- Massarotti, A., D. W. Latham, R. P. Stefanik, & J. Fogel. 2008, AJ, 135, 209
- Meyer, M. R., N. Calvet, & L. A. Hillenbrand. 1997, AJ, 114, 288M
- Mohanty, S., R. Jayawardhana, & G. Basri. 2005, ApJ, 626, 498
- Montes, D., R. González-Peinado, H. M. Tabernero, et al. 2018, MNRAS, 479, 1332
- Moraux, E. 2016, EAS Publications Series, 80-81, 73
- Murray, N. 2011, ApJ, 729, 133
- Muzerole, J., N. Calvet, & L. Hartmann. 1998, ApJ, 492, 743
- Neckel, T., & H. J. Staude. 1995, ApJ, 448, 832
- Nidever, D. L., G. W. Marcy, R. P. Butler, D. A. Fischer, & S. S. Vogt. 2002, ApJ, 141, 503
- Nisak, A., R. J. White, W. C. Jao, et al. 2021, in prep.
- Palla, F., S. Randich, E. Flaccomio, & R. Pallavicini. 2005, ApJ, 626L, 49P
- Palla, F., S. Randich, Y. V. Pavlenko, E. Flaccomio, & R. Pallavicini. 2007, ApJ, 659L, 41P
- Paredes, L., T. Henry, W. C. Jao, et al. 2021, in prep.

- Paxton, B., L. Bildsten, A. Dotter, et al. 2011 ApJS, 192, 3
- Paxton, B., M. Cantiello, P. Arras, et al. 2013, ApJS, 208, 4
- Paxton, B., P. Marchant, J. Schwab, et al. 2015, ApJS, 220, 15
- Pecaut, M. J., & E. E. Mamajek. 2013, ApJ, 208, 9, Web version 2017.09.25
- Persi, P., M. Ferrari-Toniolo, A. R. Marenzi, et al. 1994, A&A, 282, 233
- Pettersson, B. 1987, A&A, 171, 101
- Pettersson, B. B. Reipurth, ed. 2007, Astronomical Society of the Pacific, *Handbook of Star Forming Regions Vol. II*
- Purcell, C. R., B. M. Gaensler, X. H. Sun, et al. 2015, ApJ, 804, 22
- Ramírez, I., C. Allende Prieto, & D. L. Lambert. 2007, A&A, 465, 271
- Randich, S., Aharpour, N., Pallavicini, R., et al. 1997, A&A, 323, 86
- Rebull, L. M., C. H. Johnson , V. Hoette, et al. 2011, AJ, 142, 25
- Rei, A. C. S., P. P. Petrov, & J. F. Gameiro. 2017, arXiv, 1712.03784v1
- Rei, A. C. S., P. P. Petrov, & J. F. Gameiro. 2018, A&A, 610, A40
- Reipurth, B. 1983, A&A, 117, 183
- Reipurth, B., & B. Pettersson. 1993, A&A, 267, 439
- Reynolds, R. J. 1976, ApJ, 206, 679
- Rieke, G. H., & M. J. Lebofsky. 1985, ApJ, 288, 618
- Rodgers, A. W., C. T. Campbell, & J. B. Whiteoak. 1960, MNRAS, 121, 103
- Royer, F., J. Zorec, & A. E. Gómez. 2007, A&A, 463, 671
- Sabbi, E., M. Gennaro, J. Anderson, et al. 2020, ApJ, 891, 2
- Sahu, M., & K. C. Sahu. 1992, A&A, 259, 265
- Sanders, W. L. 1971, A&A, 14, 226
- Schilbach, E., & S. Röser. 2008, A&A, 489, 105
- Schröder, C., A. Reiners, & J. H. M. M. Schmitt. 2009, A&A, 493, 1099
- Shu, F. H., F. C. Adams, & S. Lizano. 1987, ARA&A, 25, 23
- Sim, G., S. H. Lee, H. B. Ann, & S. Kim. 2019, JKAS, 52, 145
- Skrutskie, M. F., R. M. Cutri, R. Stiening, et al. 2006, AJ, 131, 1163
- Soto, M. G., & J. S. Jenkins. 2018, A&A, 615, 76
- Soubiran, C., J.-F. Le Campion, N. Brouillet, & L. Chemin. 2016, A&A, 591, 118
- Soubiran, C., T. Cantat-Gaudin, M. Romero-Gomez, et al. 2018, A&A, 619, 155
- Sridharan, T. K. 1992, A&A, 13, 217
- Takeda, Y., B. Sato, E. Kambe, et al. 2005, PASJ, 57, 13
- Tokovinin, A., D. A. Fischer, M. Bonati, et al. 2013, PASP, 125, 1336
- Torres, C. A. O., G. R. Quast, L. da Silva, et al. 2006, A&A, 460, 695
- Valenti, J. A., & D. A. Fischer. 2005, ApJ, 159, 141
- Van den Bergh, S., & W. Herbst. 1975, AJ, 80, 208V
- Vogt, S. S., S. L. Allen, B. C. Bigelow, et al. 1994, Proc. SPIE, 2198, 362
- Walch, S., Whitworth, A. P., Bisbas, T. G., et al. 2013, MNRAS, 435, 917
- White, R. J., & A. M. Ghez. 2001, ApJ, 556, 265
- White, R. J., & G. Basri. 2003, ApJ, 582, 1109
- White, R. J., & L. A. Hillenbrand. 2004, ApJ, 616, 998
- Winter, A. J., C. J. Clarke, G. Rosotti, J. Ih, S. Facchini, & T. J. Haworth. 2018, MNRAS, 478, 2700
- Woermann, B., M. J. Gaylard, & R. Otrupcek. 2001, MNRAS, 325, 1213
- Yep, A. C., & R. J. White. 2020, ApJ, 889, 50
- Yep, A. C., & R. J. White. 2021, MNRAS, under review
- Zealey, W. J., Z. Ninkov, E. Rice, M. Hartley, & S. B. Tritton. 1983, ApL, 23, 119

APPENDIX

A. SPLITTING YEP 1 AND YEP 2

Yep 1 and Yep 2 are spatially close to each other, partially overlap in distance, and have similar motions. It is possible they are two components of one association. We refine their memberships in the space they are most separate, μ_α vs. Dec , using an empirical quadratic to separate the two associations (see Figure 11).

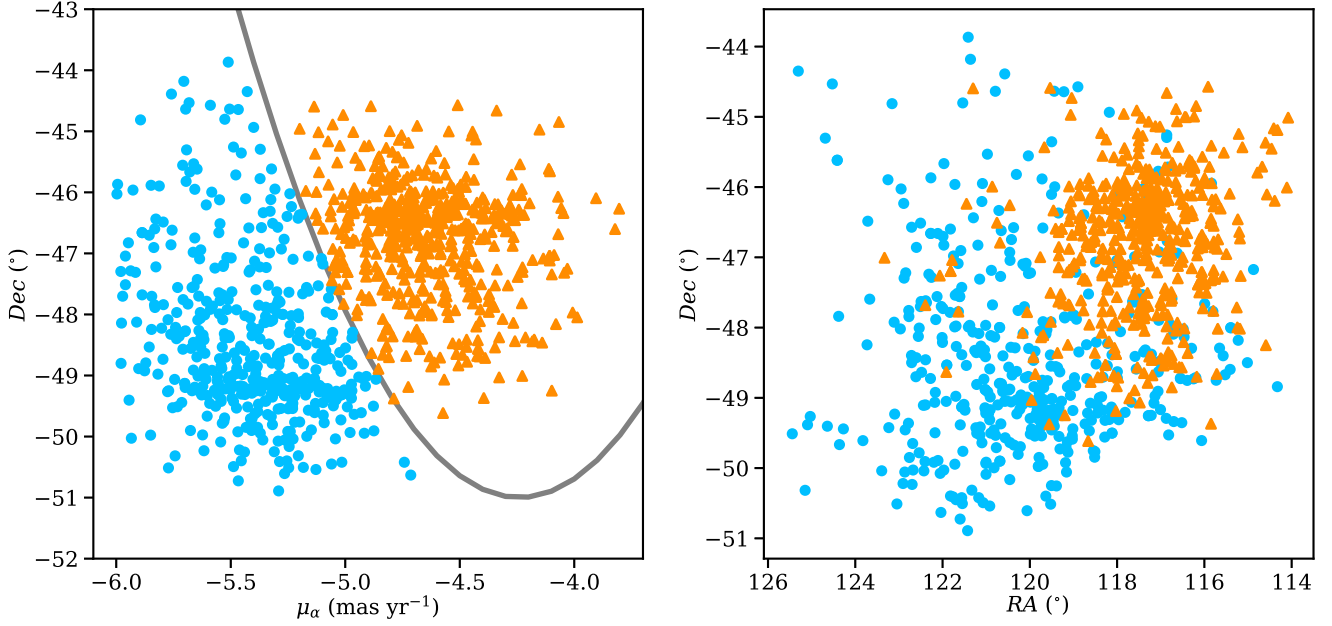


Figure 11. Associations Yep 1 (orange triangles) and Yep 2 (azule circles). We empirically split the two associations using an empirical quadratic (gray line) in μ_α vs. Dec space (left panel). The two associations spatially overlap but are distinct (right panel).